

**WORKING TITLE: UTILIZING INVARIANT MANIFOLDS OF  
CISLUNAR PERIODIC ORBITS FOR EFFICIENT DEEP  
SPACE TRANSFERS**

by

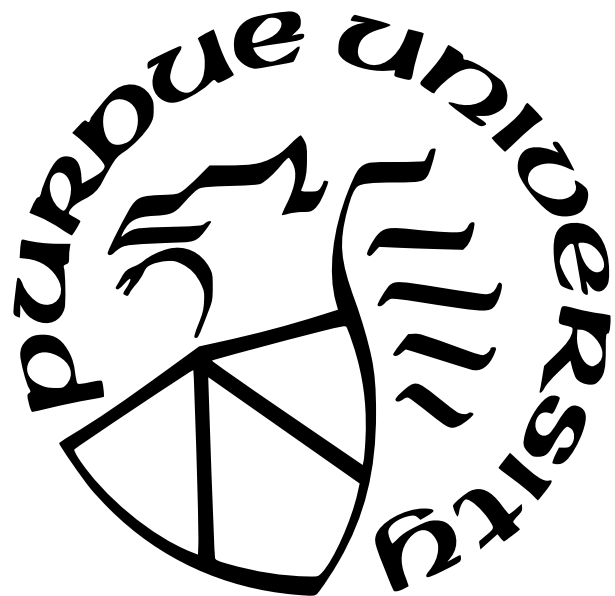
**Jonathan Richmond**

**A Thesis**

*Submitted to the Faculty of Purdue University*

*In Partial Fulfillment of the Requirements for the degree of*

**Master of Science in Aeronautics and Astronautics**



School of Aeronautics and Astronautics

West Lafayette, Indiana

May 2024

**THE PURDUE UNIVERSITY GRADUATE SCHOOL  
STATEMENT OF COMMITTEE APPROVAL**

**Dr. Kathleen C. Howell, Chair**

School of Aeronautics and Astronautics

**Dr. Carolin Frueh**

School of Aeronautics and Astronautics

**Dr. Kenshiro Oguri**

School of Aeronautics and Astronautics

**Approved by:**

Dr. Gregory A. Blaisdell

ADD DEDICATION

## **ACKNOWLEDGMENTS**

ADD ACKNOWLEDGEMENTS

## TABLE OF CONTENTS

LIST OF TABLES . . . . .	8
LIST OF FIGURES . . . . .	9
LIST OF SYMBOLS . . . . .	11
ABBREVIATIONS . . . . .	14
ABSTRACT . . . . .	15
1 INTRODUCTION . . . . .	16
1.1 Subcaption / Cleveref Testing . . . . .	16
1.1.1 Important Math . . . . .	16
1.1.2 Numbers/Units . . . . .	16
A subsubsection . . . . .	18
A paragraph . . . . .	18
1.1.3 Custom variables . . . . .	18
1.1.4 Custom colors . . . . .	18
1.1.5 Acronyms . . . . .	18
2 DYNAMICAL MODELS . . . . .	19
2.1 Coordinate Frames . . . . .	19
2.1.1 Barycentric Rotating and Inertial Frames . . . . .	19
2.1.2 The Ecliptic J2000 Primary-Centered Inertial Frame . . . . .	20
2.2 The Two-Body Problem . . . . .	21
2.2.1 Equations of Motion . . . . .	21
2.2.2 Conic Sections . . . . .	23
2.2.3 Keplerian Orbital Elements . . . . .	24
Cartesian state to Keplerian orbital elements . . . . .	24
Keplerian orbital elements to Cartesian state . . . . .	26
2.2.4 Kepler's Equation . . . . .	27
2.3 The Circular Restricted Three-Body Problem . . . . .	28
2.3.1 Equations of Motion . . . . .	28
2.3.2 Nondimensionalized Values . . . . .	29
2.3.3 Equilibrium Points . . . . .	30
2.3.4 Jacobi Constant . . . . .	31
2.4 Patched Dynamical Models . . . . .	32
2.4.1 The Patched 2BP-CR3BP Model . . . . .	32
2.4.2 The Blended CR3BP Model . . . . .	34
2.5 Coordinate Frame Transformations . . . . .	35
2.5.1 Barycentric Rotating Frame - Primary-Centric Arbitrary Inertial Frame . . . . .	35
2.5.2 Barycentric Rotating Frame - Ecliptic J2000 Inertial Frame . . . . .	37
3 CR3BP DYNAMICAL STRUCTURES . . . . .	39
3.1 Differential Corrections . . . . .	39

3.1.1	State Transition Matrix . . . . .	39
3.1.2	Multi-Variable Newton-Raphson Method . . . . .	40
3.1.3	Central Difference Method . . . . .	42
3.2	Periodic Orbits . . . . .	43
3.2.1	Lyapunov Orbits . . . . .	43
A Lyapunov Targeter . . . . .	43	
Lyapunov Initial Guess . . . . .	44	
Converged Lyapunov Orbit . . . . .	45	
Natural Parameter Continuation . . . . .	46	
3.2.2	Orbital Stability . . . . .	47
Monodromy Matrix . . . . .	47	
Stability Index . . . . .	49	
Time Constant . . . . .	49	
Bifurcations . . . . .	50	
New Family Generation from Bifurcation . . . . .	51	
3.2.3	Halo Orbits . . . . .	52
A Halo Targeter . . . . .	52	
Converged Halo Families . . . . .	53	
3.2.4	Butterfly Orbits . . . . .	54
3.2.5	Axial Orbits . . . . .	55
An Axial Targeter . . . . .	55	
Converged Axial Families . . . . .	56	
3.2.6	Vertical Orbits . . . . .	56
A Vertical Targeter . . . . .	56	
Converged Vertical Families . . . . .	58	
3.2.7	Equilateral Long Period Orbits . . . . .	59
A Planar Equilateral Orbit Targeter . . . . .	59	
Equilateral Long Period Orbit Initial Guess . . . . .	61	
Converged Equilateral Long Period Orbit Families . . . . .	61	
3.2.8	Equilateral Axial Orbits . . . . .	62
A Spatial Equilateral Orbit Targeter . . . . .	62	
Converged Equilateral Axial Families . . . . .	63	
3.2.9	Resonant Orbits . . . . .	64
Converged 2:1a Resonant Orbit Family . . . . .	64	
Converged 3:4 Resonant Orbit Family . . . . .	65	
3.3	Invariant Manifolds . . . . .	65
3.4	Poincaré Maps . . . . .	69
4	TRAJECTORY CONSTRUCTION . . . . .	72
4.1	2BP Lambert Arcs . . . . .	72
4.2	The Moon-to-Moon Analytical Transfer Method . . . . .	72
4.3	Ballistic Transfers between Earth-Moon and Sun-Earth Systems . . . . .	72
4.4	Flyby Targeting . . . . .	72
5	END-TO-END MARS TRANSFERS . . . . .	73

5.1	Transfers via Intermediate Sun-Earth Halos . . . . .	73
5.2	Direct Transfers with Flybys . . . . .	73
6	CONCLUSION . . . . .	74
	REFERENCES . . . . .	75

## LIST OF TABLES

1.1	Sample Table . . . . .	17
2.1	Characteristic Values of Relevant CR3BP Systems . . . . .	30
3.1	Manifold Step-Off Distance Values of Relevant CR3BP Systems . . . . .	69

## LIST OF FIGURES

1.1	Two images of Orion: (a) and (b) . . . . .	17
2.1	Barycentric rotating and inertial frames in a CR3BP system. . . . .	20
2.2	Earth-centered Ecliptic J2000 inertial frame. . . . .	21
2.3	Two-body problem in a barycentric inertial frame. . . . .	22
2.4	Orientation and location along an orbit in an inertial frame using Keplerian orbital elements. . . . .	25
2.5	Definition of eccentric anomaly and the auxiliary circle. . . . .	26
2.6	CR3BP barycentric rotating frame with Lagrange points. . . . .	31
2.7	<i>XY</i> -Projection of the Patched 2BP-CR3BP Model . . . . .	33
2.8	<i>xy</i> -Projection of the Blended CR3BP Model . . . . .	35
3.1	Simple Targeting Example. . . . .	42
3.2	Converged periodic Lyapunov orbit in the Earth-Moon barycentric rotating frame. . . . .	46
3.3	Earth-Moon $L_1$ Lyapunov orbit family. . . . .	47
3.4	Earth-Moon $L_2$ Lyapunov orbit family. . . . .	48
3.5	Earth-Moon Lyapunov family stability index evolution. . . . .	50
3.6	Earth-Moon Lyapunov family time constant evolution. . . . .	50
3.7	Earth-Moon $L_1$ southern halo orbit family. . . . .	53
3.8	Earth-Moon $L_2$ southern halo orbit family. . . . .	54
3.9	Earth-Moon Halo family stability index evolution. . . . .	54
3.10	Earth-Moon butterfly family. . . . .	55
3.11	Earth-Moon butterfly family stability index evolution. . . . .	56
3.12	Earth-Moon $L_1$ northeast axial orbit family. . . . .	57
3.13	Earth-Moon $L_2$ northwest axial orbit family. . . . .	58
3.14	Earth-Moon axial family stability index evolution. . . . .	58
3.15	Earth-Moon $L_1$ vertical orbit family. . . . .	59
3.16	Earth-Moon $L_2$ vertical orbit family. . . . .	60
3.17	Earth-Moon vertical family stability index evolution. . . . .	60
3.18	Earth-Moon $L_4$ and $L_5$ equilateral long period orbit families. . . . .	62

3.19	Earth-Moon equilateral long period orbit family stability index evolution. . . . .	63
3.20	Earth-Moon $L_4$ and $L_5$ equilateral axial families. . . . .	64
3.21	Earth-Moon equilateral axial family stability index evolution. . . . .	65
3.22	Earth-Moon 2:1a resonant orbit family. . . . .	66
3.23	Earth-Moon 2:1a resonant orbit family stability index evolution. . . . .	67
3.24	Earth-Moon 3:4 resonant orbit family. . . . .	68
3.25	Earth-Moon 3:4 resonant orbit family stability index evolution. . . . .	69
3.26	Earth-Moon $L_1$ Lyapunov Manifolds ( $C = 3.05$ ). . . . .	70
3.27	Earth-Moon $L_2$ Halo Manifolds ( $C = 3.08$ ). . . . .	71
3.28	Poincaré map. . . . .	71

## LIST OF SYMBOLS

*Variables*

$a$	Semimajor axis [km]
$B$	Barycenter
$C$	Jacobi constant
$DF$	Jacobian matrix
$d$	Manifold step-off distance
$d_{SOI}$	Sphere of influence gravitational ratio
$E$	Eccentric anomaly [rad (deg)]
$\mathcal{E}$	Specific mechanical energy [ $\text{km}^2/\text{s}^2$ ]
$e$	Eccentricity
$\bar{e}$	Eccentricity vector in $\mathbb{R}^3$
$\bar{F}$	Constraint vector
$\bar{F}_g$	Gravitational force vector in $\mathbb{R}^3$ [kN]
$G$	Universal gravitational constant [kN*km <sup>2</sup> /kg <sup>2</sup> ]
$\tilde{G}$	Normalized gravitational constant
$g$	Gravitational acceleration
$\bar{h}$	Specific angular momentum vector in $\mathbb{R}^3$ [km <sup>2</sup> /s]
$i$	Inclination [rad (deg)]
$L$	Lagrange (equilibrium) point
$l^*$	Characteristic length [km]
$M$	Mean anomaly [rad (deg)]
$m$	Mass [kg]
$m^*$	Characteristic mass [kg]
$n$	Mean motion [rad/s (deg/s)]
$\tilde{n}$	Normalized mean motion
$\bar{n}$	Node vector in $\mathbb{R}^3$
$P$	Primary
$\mathbb{P}$	Period [s]

$\bar{Q}$	Inertial state vector in $\mathbb{R}^6$
$\bar{q}$	Rotating state vector in $\mathbb{R}^6$
$\bar{R}$	Inertial position vector in $\mathbb{R}^3$ [km]
$r$	Distance [kg]
$\bar{r}$	Position vector in $\mathbb{R}^3$ [km]
$\dot{\bar{r}}$	Velocity vector in $\mathbb{R}^3$ [km/s]
$\ddot{\bar{r}}$	Acceleration vector in $\mathbb{R}^3$ [km/s <sup>2</sup> ]
$r_a$	Radius of apoapsis [km]
$r_p$	Radius of periapsis [km]
$s/c$	Spacecraft
$t$	Time [s]
$t^*$	Characteristic time [s]
$U$	Pseudo-potential
$v$	Velocity [km/s]
$v_r$	Radial velocity [lm/s]
$X$	Position along the $\hat{X}$ -axis in an inertial frame [km]
$\bar{X}$	Free variable vector
$\ddot{X}$	Acceleration along the $\hat{X}$ -axis in an inertial frame [km/s <sup>2</sup> ]
$x$	Position along the $\hat{x}$ -axis in a rotating frame
$\dot{x}$	Velocity along the $\hat{x}$ -axis in a rotating frame
$\ddot{x}$	Acceleration along the $\hat{x}$ -axis in a rotating frame
$Y$	Position along the $\hat{Y}$ -axis in an inertial frame [km]
$\ddot{Y}$	Acceleration along the $\hat{Y}$ -axis in an inertial frame [km/s <sup>2</sup> ]
$y$	Position along the $\hat{y}$ -axis in a rotating frame
$\dot{y}$	Velocity along the $\hat{y}$ -axis in a rotating frame
$\ddot{y}$	Acceleration along the $\hat{y}$ -axis in a rotating frame
$Z$	Position along the $\hat{Z}$ -axis in an inertial frame [km]
$\ddot{Z}$	Acceleration along the $\hat{Z}$ -axis in an inertial frame [km/s <sup>2</sup> ]
$z$	Position along the $\hat{z}$ -axis in a rotating frame

$\dot{z}$	Velocity along the $\hat{z}$ -axis in a rotating frame
$\ddot{z}$	Acceleration along the $\hat{z}$ -axis in a rotating frame
$\Delta v$	Change in velocity that characterizes a maneuver
$\epsilon$	Machine tolerance
$\theta$	True anomaly [rad (deg)]
$\kappa$	Small perturbation
$\lambda$	Eigenvalue
$\mu$	CR3BP mass ratio
$\mu_{2BP}$	Two-body gravitational constant [ $\text{kN}^*\text{km}^2/\text{kg}$ ]
$\bar{\nu}$	Eigenvector in $\mathbb{R}^6$
$\bar{P}$	Inertial position vector in $\mathbb{R}^3$
$\dot{\rho}$	Barycentric rotating velocity
$\bar{\rho}$	Barycentric rotating position vector in $\mathbb{R}^3$
$\dot{\bar{\rho}}$	Barycentric rotating velocity vector in $\mathbb{R}^3$
$\varsigma$	Stability index
$\tau$	Time
$\Upsilon$	Time constant
$\Phi$	State transition matrix
$\phi$	State transition matrix element
$\Omega$	Right ascension of ascending node (RAAN) [rad (deg)]
$\omega$	Argument of periapsis [rad (deg)]
$\bar{\omega}$	Angular velocity vector in $\mathbb{R}^3$

#### *Coordinate Frames*

$\{\hat{X}, \hat{Y}, \hat{Z}\}$	Arbitrary inertial coordinate frame
$\{\hat{X}_{Ec}, \hat{Y}_{Ec}, \hat{Z}_{Ec}\}$	Ecliptic J2000 inertial coordinate frame
$\{\hat{x}, \hat{y}, \hat{z}\}$	Rotating coordinate frame

## ABBREVIATIONS

2BP	2-Body Problem
BCR4BP	Bicircular Restricted 4-Body Problem
CR3BP	Circular Restricted 3-Body Problem
HFEM	High-fidelity ephemeris model
HR4BP	Hills Restricted 4-Body Problem
NAIF	Navigation and Ancillary Information Facility
NASA	National Aeronautics and Space Administration
QBCR4BP	Quasi-Bicircular Restricted 4-Body Problem
RAAN	Right ascension of ascending node
SoI	Sphere of influence
STM	State transition matrix
SVD	Singular value decomposition
TOF	Time-of-flight

## **ABSTRACT**

ADD ABSTRACT

# 1. INTRODUCTION

Experimenting with the available typographic conventions defined in the Purdue file:

`pa-typographic-conventions.sty`: these include *Emph First Title* `Keys` `Literal` `Menu` `Open menu` `Preferences` `Shell.sh`. Now let's try out a footnote<sup>1</sup>, one of the fancy TODO notes , and more scary TODO , as well as a a todo error as well as a citation [1]. Note the TODO comments currently only show up in `quick` or `debug` modes (for now).

## 1.1 Subcaption / Cleveref Testing

Here is a very important and informative figure for Orion. You can see in Figure 1.1 that there is both Figure 1.1(a) and Figure 1.1(b)! There is also important information in Table 1.1. If you're confused, then Equation (1.1) should clarify things. Some other ways to put it: Equations (1.1) and (1.2) and Equations (1.1) to (1.3).

### 1.1.1 Important Math

$$e^{i\pi} + 1 = 0 \tag{1.1}$$

$$a^2 + b^2 = c^2 \tag{1.2}$$

$$\frac{df}{dt} = \lim_{h \rightarrow 0} \frac{f(t+h) - f(t)}{h} \tag{1.3}$$

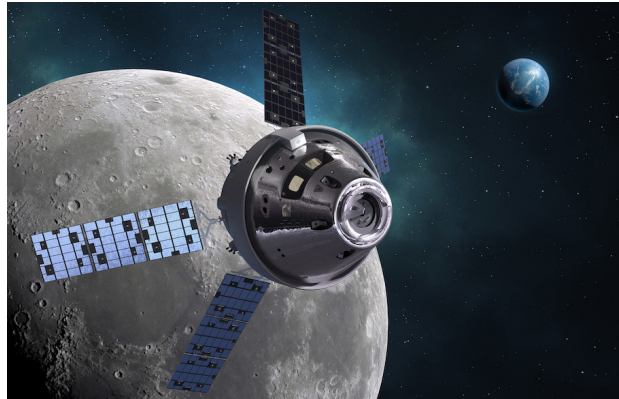
### 1.1.2 Numbers/Units

Some of the number formats available:  $-10^{10}$ .  $2 \times 4$ . 10 to 11.  $12.3^\circ$ .

Experimenting with the siunits package:  $8 \text{ kg m s}^{-2}$ .  $9\text{N}$ .  $2.3 \times 10^{27} \text{ kg}$ .  $1.345 \frac{\text{C}}{\text{mol}}$ .

---

<sup>1</sup>↑I'm a footnote!



(a) Orion 1



(b) Orion 2

**Figure 1.1.** Two images of Orion: (a) and (b).

**Table 1.1.** Sample Table

Sample	Table
$x$	2

## A subsubsection

A subsubsection for testing out the table of contents

## A paragraph

What happens for a paragraph in the table of contents?

### 1.1.3 Custom variables

Variables can be defined as functions in [t0-template](#) ↗ [te4-custom-variables.tex](#)

The rotating  $x$  axis is clearly the best of all axes. But even better is the  $\mathbf{x}$  vector and the  $\hat{x}$  direction! See the appendix in Debug mode for details

### 1.1.4 Custom colors

There are a variety of available colors from Purdue's branding<sup>2</sup> like: Boilermaker Gold, Rush. This example document also include the Tableau colors<sup>3</sup>. For example, `tab-blue` and `tab-red`.

### 1.1.5 Acronyms

Acronyms handled through `glossaries`, and defined in [t0-template](#) ↗ [te6-acronyms.tex](#). For example, the first time we will refer to the Circular Restricted Three Body Problem (CR3BP), and in the future only say CR3BP.

---

<sup>2</sup>↑see <https://marcom.purdue.edu/our-brand/visual-identity/>

<sup>3</sup>↑used in matplotlib - [https://matplotlib.org/3.4.1/gallery/color/named\\_colors.html](https://matplotlib.org/3.4.1/gallery/color/named_colors.html)

## 2. DYNAMICAL MODELS

This analysis relies on the utilization of two primary dynamical models: The Two-Body Problem (2BP) and the Circular Restricted Three-Body Problem (CR3BP). The 2BP serves as a model for spacecraft dynamics when their motion is solely governed by the gravitational influence of a single body, primarily applied to the study of heliocentric arcs within this investigation. In cases where the dynamics are significantly influenced by the gravitational forces of two bodies, as exemplified in Sun-planet or the Earth-Moon systems, the CR3BP offers a more accurate description of the spacecraft's motion.

### 2.1 Coordinate Frames

In this investigation, Cartesian coordinate frames are employed to represent three-dimensional vector quantities. These frames may remain fixed in space (inertial) or rotate about the origin at a constant angular rate (rotating). The choice of coordinate frame depends on the specific application as it can be advantageous to position the origin at the center of mass of the system (barycenter) or align it with a primary body of interest.

#### 2.1.1 Barycentric Rotating and Inertial Frames

In a CR3BP system, the motion of a spacecraft is best depicted within a rotating frame with its origin at the system barycenter. The  $\hat{x}$ -axis is defined to extend from the barycenter toward the smaller primary body, while the  $\hat{z}$ -axis aligns with the system's angular momentum vector. Completing the triad, the  $\hat{y}$ -axis is  $\hat{y} = \hat{z} \times \hat{x}$ . This frame rotates about the barycenter at a constant angular rate identical to that of the primary bodies.

Additionally, an arbitrary barycentric inertial frame can be similarly defined using the rotating axes at a specific instance in time, denoted as  $\hat{X}$ ,  $\hat{Y}$ , and  $\hat{Z}$ . As time progresses, the inertial frame remains fixed in space, whereas the rotating frame revolves around the shared origin with the primaries. In Figure 2.1, the barycentric  $\{\hat{x}, \hat{y}, \hat{z}\}$  rotating frame and  $\{\hat{X}, \hat{Y}, \hat{Z}\}$  inertial frames for an example CR3BP system are illustrated, with their common origin centered at the barycenter of the primaries,  $P_1$  and  $P_2$ . The angle between the two

frames is denoted here by  $\theta$  and it increases at a constant rate of  $n$ . It is important to note that both the  $\hat{Z}$ - and  $\hat{z}$ -axes adhere to the right-hand frame convention, pointing out of the page.

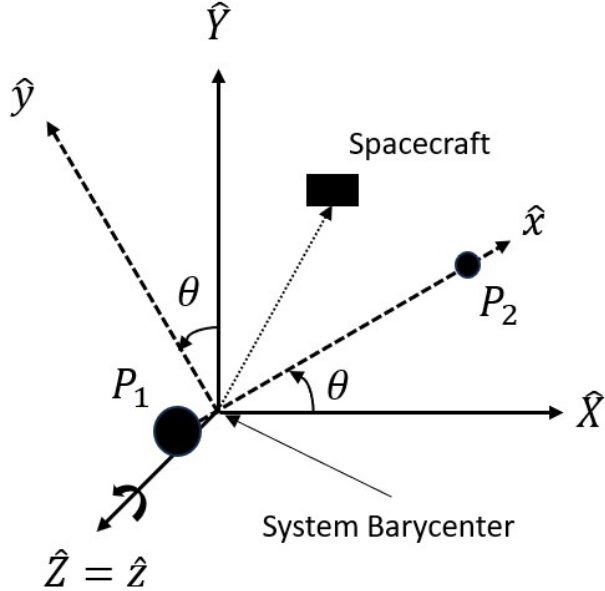


**Figure 2.1.** Barycentric rotating and inertial frames in a CR3BP system.

### 2.1.2 The Ecliptic J2000 Primary-Centered Inertial Frame

A commonly used primary-centered inertial frame is the Ecliptic J2000. As the name implies, this frame is established with its origin at the center of a primary body and the Sun-Earth orbital plane on January 1, 2000 as the  $\hat{X}_{Ec}\hat{Y}_{Ec}$ -plane. The  $\hat{X}_{Ec}$ -axis is directed towards the vernal equinox, which is the line of intersection between the Earth's equatorial and ecliptic planes on January 1, 2000. The  $\hat{Z}_{Ec}$ -axis is orthogonal to the ecliptic plane, and the  $\hat{Y}_{Ec}$ -axis completes the triad, defined as  $\hat{Y}_{Ec} = \hat{Z}_{Ec} \times \hat{X}_{Ec}$ .

Since the frame is centered on a primary, it applies to both the 2BP and CR3BP, making it also valuable for patched dynamical models. The construction of this coordinate frame, as depicted in Figure 2.2, is computed using the Navigation and Ancillary Information Facility's (NAIF) SPICE ephemeris toolkit[2].

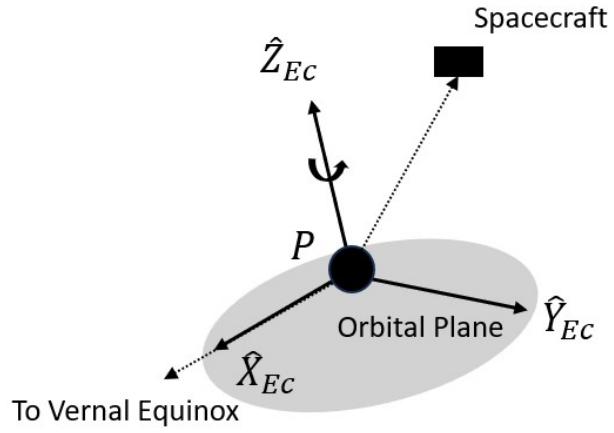


**Figure 2.2.** Earth-centered Ecliptic J2000 inertial frame.

## 2.2 The Two-Body Problem

This investigation treats the motion of spacecraft in heliocentric space, specifically when they are far from planets and moons, as a Two-Body Problem, governed by a single gravitational force. This section provides a brief overview of key aspects of 2BP dynamics, Keplerian orbital elements, and Kepler's Equation. For a more comprehensive derivation of the 2BP, refer to Chapters 1 and 2 of Vallado's *Fundamentals of Astrodynamics and Applications*[3]. Additionally, Canales highlights the background information relevant to understanding the transfer methodologies presented in this analysis[4].

### 2.2.1 Equations of Motion

The 2BP involves two point masses—a primary body and a spacecraft—that exert gravitational forces on each other. Since no external forces act on this system, the center of mass of the bodies moves at a constant velocity and serves as the origin for an inertial coordinate frame. In this inertial frame, the gravitational force that the primary body exerts on the spacecraft, denoted as  $\bar{F}_{g_{P \rightarrow s/c}}$ , is expressed as:

$$\bar{F}_{g_{P \rightarrow s/c}} = -\frac{Gm_P m_{s/c}}{r_{P \rightarrow s/c}^3} \bar{r}_{P \rightarrow s/c}, \quad (2.1)$$

where  $G$  is the universal gravitational constant ( $6.67384 \times 10^{-20}$  kN\*km $^2$ /kg $^2$ ),  $m_P$  and  $m_S$  are the masses of the primary body and spacecraft, respectively,  $r_{P \rightarrow s/c}$  is the distance from the primary body to the spacecraft, and  $\bar{r}_{P \rightarrow s/c} = \bar{r}_{s/c} - \bar{r}_P$  is the position vector from the primary body to the spacecraft in the inertial frame, as illustrated in Figure 2.3.

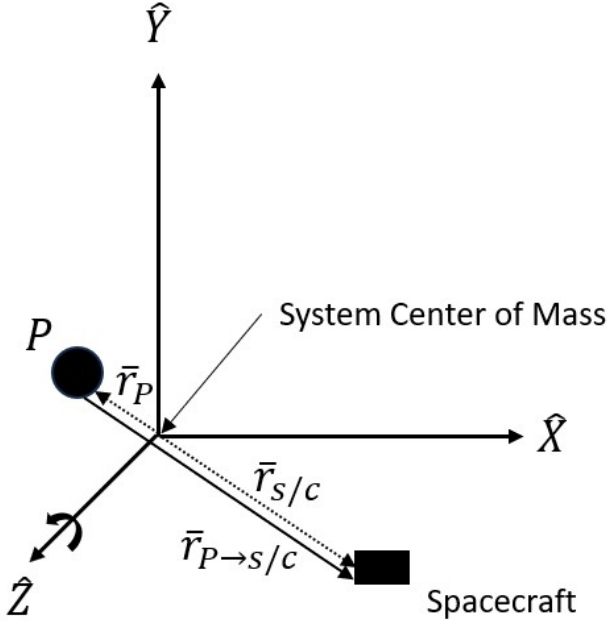


**Figure 2.3.** Two-body problem in a barycentric inertial frame.

Assuming that the mass of the spacecraft is negligible compared to the mass of the primary body, the nonlinear relative equation of motion for the 2BP is derived[3], [4]:

$$\ddot{\bar{r}}_{P \rightarrow s/c} = -\frac{\mu_{2BP}}{r_{P \rightarrow s/c}^3} \bar{r}_{P \rightarrow s/c}, \quad (2.2)$$

where  $\ddot{\bar{r}}_{P \rightarrow s/c}$  is the inertial acceleration of the spacecraft relative to the primary body and  $\mu_{2BP} = Gm_P$ . This vector equation can also be expressed as  $\hat{X}$ ,  $\hat{Y}$ , and  $\hat{Z}$  scalar equations in the inertial frame:

$$\ddot{X} = -\frac{\mu_{2BP}}{r_{P \rightarrow s/c}^3} (X_{s/c} - X_P), \quad (2.3)$$

$$\ddot{Y} = -\frac{\mu_{2BP}}{r_{P \rightarrow s/c}^3} (Y_{s/c} - Y_P), \quad (2.4)$$

$$\ddot{Z} = -\frac{\mu_{2BP}}{r_{P \rightarrow s/c}^3} (Z_{s/c} - Z_P). \quad (2.5)$$

### 2.2.2 Conic Sections

Instead of relying on numerical propagation of the nonlinear equations of motion, space-craft motion in the 2BP can be effectively represented analytically using conic sections. This section provides a concise overview of conic motion in the 2BP.

Two essential constants characterize conic orbits: specific angular momentum  $\bar{h}$  and specific mechanical energy  $\mathcal{E}$ :

$$\bar{h} = \bar{r}_{P \rightarrow s/c} \times \dot{\bar{r}}_{P \rightarrow s/c}, \quad (2.6)$$

$$\mathcal{E} = \frac{v_{P \rightarrow s/c}^2}{2} - \frac{\mu_{2BP}}{r_{P \rightarrow s/c}}, \quad (2.7)$$

where  $v_{P \rightarrow s/c} = \|\dot{\bar{r}}_{P \rightarrow s/c}\|_2$  is the spacecraft velocity in the inertial frame relative to the primary body.

Kepler's first law, asserting that orbital motion is conic, provides the trajectory equation for the 2BP:

$$r_{P \rightarrow s/c} = \frac{a(1 - e^2)}{1 + e \cos(\theta)}, \quad (2.8)$$

where  $a$  represents the orbit semimajor axis,  $e$  is the orbit eccentricity, and  $\theta$  denotes the orbit true anomaly. These three elements will be elaborated upon in a later subsection. Equation (2.8) can also be employed to compute the periapsis and apoapsis distances,  $r_p$  and  $r_a$  respectively:

$$r_p = a(1 - e), \quad (2.9)$$

$$r_a = a(1 + e). \quad (2.10)$$

The eccentricity can also be used to determine the type of conic section:

- $e = 0$ : Circular orbit (a special case of an ellipse).
- $0 < e < 1$ : Elliptical orbit.
- $e = 1$ : Parabola.
- $e > 1$ : Hyperbola.

This investigation focuses on circles and ellipses with  $0 \leq e < 1$ .

Similarly, Kepler's third law provides the orbit period  $\mathbb{P}$  and, consequently, the mean motion  $n$ :

$$\mathbb{P} = 2\pi \sqrt{\frac{a^3}{\mu_{2BP}}}, \quad (2.11)$$

$$n = \frac{2\pi}{\mathbb{P}} = \sqrt{\frac{\mu_{2BP}}{a^3}}. \quad (2.12)$$

### 2.2.3 Keplerian Orbital Elements

Instead of specifying the six-dimensional state of a spacecraft in a 2BP elliptical orbit using Cartesian coordinates, six orbital elements can be employed to articulate the size, shape, orientation, and current location along the orbit. In addition to the semimajor axis  $a$  and eccentricity  $e$ , which were introduced earlier and describe the size and shape of the ellipse, three angles characterize the orientation of the orbit with respect to an inertial frame, as depicted in Figure 2.4:

- **Inclination**  $i$  signifies the tilt of the orbital plane relative to the inertial  $\hat{X}_{Ec}\hat{Y}_{Ec}$ -plane.
- **Right ascension of the ascending node** (RAAN)  $\Omega$  denotes the angle between the  $\hat{X}_{Ec}$ -axis and the ascending node, where the orbit crosses the  $\hat{X}_{Ec}\hat{Y}_{Ec}$ -plane in the positive  $\hat{Z}_{Ec}$  direction.
- **Argument of periapsis**  $\omega$  is the angle between the ascending node and the periapsis.

Finally, the true anomaly  $\theta$  defines the spacecraft's position relative to the orbit's periapsis.

#### Cartesian state to Keplerian orbital elements

To convert from a Cartesian state vector to Keplerian orbital elements, start by calculating the inclination from angular momentum:

$$i = \arccos\left(\frac{h_z}{\|\bar{h}\|}\right) \quad (2.13)$$

Using the node vector  $\bar{n}$ :

$$\bar{n} = \hat{Z}_{Ec} \times \bar{h}, \quad (2.14)$$

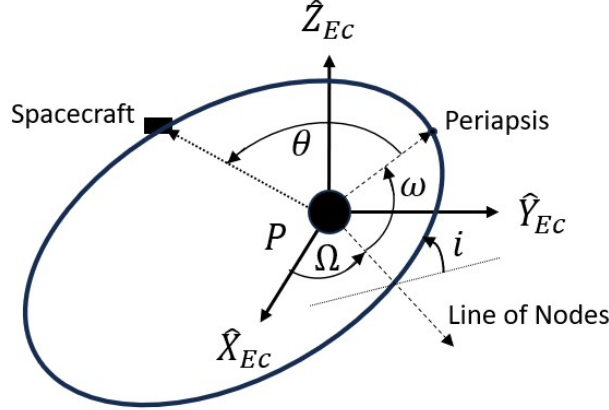


**Figure 2.4.** Orientation and location along an orbit in an inertial frame using Keplerian orbital elements.

the RAAN becomes:

$$\Omega = \begin{cases} \arccos\left(\frac{n_X}{\|\bar{n}\|}\right) & n_Y \geq 0 \\ 2\pi - \arccos\left(\frac{n_X}{\|\bar{n}\|}\right) & n_Y < 0 \end{cases}. \quad (2.15)$$

The eccentricity vector  $\bar{e}$  is also calculated from the angular momentum:

$$\bar{e} = \frac{\dot{\bar{r}}_{P \rightarrow s/c} \times \bar{h}}{\mu_{2BP}} - \frac{\bar{r}_{P \rightarrow s/c}}{r_{P \rightarrow s/c}}, \quad (2.16)$$

and

$$e = \|\bar{e}\|. \quad (2.17)$$

The remaining three orbital elements are calculated as follows:

$$a = \frac{\|\bar{h}\|}{\mu_{2BP}(1 - e^2)}, \quad (2.18)$$

$$\omega = \begin{cases} \arccos\left(\frac{\bar{n} \cdot \bar{e}}{\|\bar{n}\|e}\right) & e_Z \geq 0 \\ 2\pi - \arccos\left(\frac{\bar{n} \cdot \bar{e}}{\|\bar{n}\|e}\right) & e_Z < 0 \end{cases}, \quad (2.19)$$

$$\theta = \begin{cases} \arccos\left(\frac{\bar{e} \cdot \bar{r}_{P \rightarrow s/c}}{e r_{P \rightarrow s/c}}\right) & v_r \geq 0 \\ 2\pi - \arccos\left(\frac{\bar{e} \cdot \bar{r}_{P \rightarrow s/c}}{e r_{P \rightarrow s/c}}\right) & v_r < 0 \end{cases}, \quad (2.20)$$

where

$$v_r = \frac{\dot{r}_{P \rightarrow s/c} \cdot \bar{r}_{P \rightarrow s/c}}{r_{P \rightarrow s/c}}. \quad (2.21)$$

### Keplerian orbital elements to Cartesian state

Similarly, the Cartesian state vector can be obtained from the Keplerian orbital elements. First, the eccentric anomaly  $E$  is needed, which is the angle made by the eccentricity vector pointing to periapsis and the vector from the center of the ellipse to the point directly above the spacecraft location (perpendicular to the eccentricity vector) on an auxiliary circle drawn tangent to the ellipse. The eccentric anomaly and the auxiliary circle are illustrated in Figure 2.5, along with the eccentricity vector and semimajor axis.

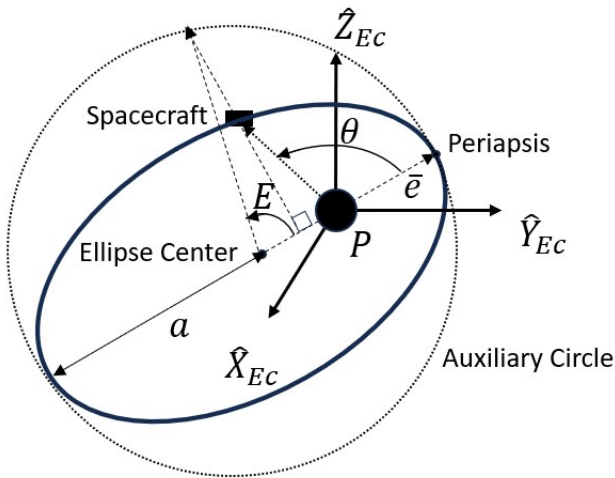


**Figure 2.5.** Definition of eccentric anomaly and the auxiliary circle.

The eccentric anomaly can be related to the true anomaly,

$$E = \arctan\left(\frac{\sqrt{1-e^2}\sin(\theta)}{e + \cos(\theta)}\right), \quad (2.22)$$

which can then be used to calculate the distance from the primary:

$$r_{P \rightarrow s/c} = a(1 - e \cos(E)). \quad (2.23)$$

This can be used to generate position and velocity magnitude vectors:

$$\bar{r}_0 = \begin{bmatrix} r_{P \rightarrow s/c} \cos(\theta) \\ r_{P \rightarrow s/c} \sin(\theta) \\ 0 \end{bmatrix}, \quad (2.24)$$

$$\dot{\bar{r}}_0 = \sqrt{\frac{\mu_{2BPA}}{r_{P \rightarrow s/c}}} \begin{bmatrix} -\sin(E) \\ \sqrt{1-e^2} \cos(E) \\ 0 \end{bmatrix}. \quad (2.25)$$

These vectors will need to be rotated relative to the inertial frame axes according to the inclination, RAAN, and argument of periapsis:

$$C = \begin{bmatrix} \cos(\Omega) \cos(\omega) - \cos(i) \sin(\Omega) \sin(\omega) & -\cos(\Omega) \sin(\omega) - \cos(i) \sin(\Omega) \cos(\omega) & 0 \\ \sin(\Omega) \cos(\omega) + \cos(i) \cos(\Omega) \sin(\omega) & -\sin(\Omega) \sin(\omega) + \cos(i) \cos(\Omega) \cos(\omega) & 0 \\ \sin(i) \sin(\omega) & \sin(i) \cos(\omega) & 0 \end{bmatrix}, \quad (2.26)$$

$$\bar{r}_{P \rightarrow s/c} = C \bar{r}_0, \quad (2.27)$$

$$\dot{\bar{r}}_{P \rightarrow s/c} = C \dot{\bar{r}}_0. \quad (2.28)$$

## 2.2.4 Kepler's Equation

If the difference in true anomaly between two points on an orbit is known, Kepler's equation becomes a valuable tool for calculating the time-of-flight between these points. The mean anomaly  $M$  serves as a measure of how much of the orbit has been traversed past periapsis with respect to time:

$$M = \frac{2\pi(t - t_p)}{P}, \quad (2.29)$$

where  $(t - t_p)$  represents the time since periapsis.

Kepler's equation establishes a connection between the mean and eccentric anomalies, thereby linking the eccentric anomaly to time:

$$M = E - e \sin(E). \quad (2.30)$$

To determine eccentric anomalies given corresponding true anomalies, employ Equation (2.22), and subsequently, using Kepler's equation (Equation (2.30)), convert them to mean anomalies. The difference in mean anomalies with Equation (2.29) provides the time-of-flight between the two points along the orbit.

## 2.3 The Circular Restricted Three-Body Problem

When a spacecraft is significantly impacted by the gravitational force of two celestial bodies the Circular Restricted 3-Body Problem better approximates the spacecraft's motion compared to two-body problems. Therefore, this investigation uses the CR3BP to model the Earth-Moon and Sun-planet systems when appropriate. The CR3BP is an autonomous model (its dynamics are time-invariant) that provides insight into the dynamical structures present in the system without some of the complexities of a higher-fidelity ephemeris model.

### 2.3.1 Equations of Motion

The CR3BP consists of three primary bodies, two celestial bodies and a massless spacecraft. The two celestial bodies exert gravitational forces on each other and the satellite; however, the satellite does not affect the other two bodies.

The two celestial bodies are treated as point masses and assumed to move in circular orbits, with a constant angular velocity, around their barycenter  $B$ . Assuming that no other forces are acting on the system,  $B$  can be considered an inertial point, and similar to the 2BP, Newton's Laws can be expressed relative to that point. Unlike the 2BP, there is currently no analytical solution to represent the dynamics of the CR3BP. Consequently, all trajectories in this model must be numerically propagated in time using nonlinear, coupled equations of motion.

It is also useful and common practice to represent these equations and visualize them in a barycentric rotating coordinate frame,  $\{\hat{x}, \hat{y}, \hat{z}\}$ , as shown by the dashed lines in Figure 2.1 and described in Section 2.1. In this frame, the two celestial primaries remain fixed, while the spacecraft moves relative to them in three-dimensional configuration space.

A single mass ratio  $\mu$  characterizes a CR3BP system:

$$\mu = \frac{m_2}{m_1 + m_2}, \quad (2.31)$$

where  $m_1$  and  $m_2$  are the masses of the larger and smaller celestial primaries, respectively. In the barycentric rotating frame,  $P_1$  is located at  $x = -\mu$  and  $P_2$  is located at  $x = 1 - \mu$ . Using this parameter, a pseudo-potential function  $U$  describes the gravitational forces on the system expressed in the barycentric rotating frame:

$$U = \frac{1}{2}(x^2 + y^2) + \frac{1 - \mu}{d} + \frac{\mu}{r}, \quad (2.32)$$

$$d = \sqrt{(x + \mu)^2 + y^2 + z^2}, \quad (2.33)$$

$$r = \sqrt{(x - 1 + \mu)^2 + y^2 + z^2}, \quad (2.34)$$

where here,  $d$  and  $r$  are the distances from  $P_1$  and  $P_2$ , respectively. From the pseudo-potential, the scalar nonlinear equations of motion are expressed in the barycentric rotating frame:

$$\ddot{x} = 2\dot{y} + \frac{\partial U}{\partial x} = 2\dot{y} + x - \frac{(1 - \mu)(x + \mu)}{d^3} - \frac{\mu(x - 1 + \mu)}{r^3}, \quad (2.35)$$

$$\ddot{y} = -2\dot{x} + \frac{\partial U}{\partial y} = -2\dot{x} + y - \frac{(1 - \mu)y}{d^3} - \frac{\mu y}{r^3}, \quad (2.36)$$

$$\ddot{z} = \frac{\partial U}{\partial z} = -\frac{(1 - \mu)z}{d^3} - \frac{\mu z}{r^3}. \quad (2.37)$$

Many authors provide detailed derivations for these equations of motion; one useful reference is Zimovan's Ph.D. dissertation[5].

### 2.3.2 Nondimensionalized Values

Since planetary systems deal with massive distance and velocity scales, it is often helpful in computations to use normalized length, time, and mass values with nondimensional units. Each CR3BP system has characteristic values that are used in this normalization process:

- **Characteristic length  $l^*$**  is the distance between the celestial primaries.

- **Characteristic time**  $t^*$  is selected so that the mean motion of these primaries is unity ( $\tilde{n} = 1$ ). This results in the primaries having circular orbital periods of  $2\pi$  nondimensional units.
- **Characteristic mass**  $m^*$  is the sum of the masses of these two bodies.

These definitions result in the following equations:

$$l^* = r_{12}, \quad (2.38)$$

$$m^* = m_1 + m_2, \quad (2.39)$$

$$t^* = \sqrt{\frac{l^{*3}}{Gm^*}}, \quad (2.40)$$

$$\tilde{G} = G \frac{l^{*3}}{m^* t^{*2}} = 1, \quad (2.41)$$

which are used to normalize all dimensional values in the problem. Table 2.1 shows the mass ratios and characteristic values for the three CR3BP systems used in this investigation.

**Table 2.1.** Characteristic Values of Relevant CR3BP Systems

CR3BP System	$\mu$	$l^* [\text{km}]$	$t^* [\text{s}]$	$m^* [\text{kg}]$
Earth-Moon	$1.21506 \times 10^{-2}$	$3.84748 \times 10^5$	$3.75700 \times 10^5$	$6.04604 \times 10^{24}$
Sun-Earth	$3.00348 \times 10^{-6}$	$1.49598 \times 10^8$	$5.02264 \times 10^6$	$1.98855 \times 10^{30}$
Sun-Mars	$3.22715 \times 10^{-7}$	$2.27941 \times 10^8$	$9.44664 \times 10^6$	$1.98855 \times 10^{30}$

### 2.3.3 Equilibrium Points

In the barycentric rotating frame, there are five equilibrium points (also called libration or Lagrange points) where there is no net acceleration (i.e., the pseudo-potential acceleration is balanced by the centrifugal acceleration). Thus, a spacecraft at these positions with no initial velocity would remain stationary in this model. All five Lagrange points lie in the  $xy$ -plane. Three Lagrange points lie along the axis of the two celestial primaries and are called the collinear equilibrium points:  $L_1$  is between the two bodies,  $L_2$  is past the smaller body, and  $L_3$  is past the larger body. A Newton-Raphson algorithm can be used to find the location of these points for a given mass ratio.  $L_4$  and  $L_5$  are equilateral equilibrium

points because they form equilateral triangles with the primary bodies. Their locations can be determined through geometric relationships. The energy level (or corresponding Jacobi constant, introduced in the next section) increases through points 1-4 ( $L_4$  and  $L_5$  are at the same energy level). Figure 2.6 shows the layout of the Lagrange points in a generic CR3BP barycentric rotating frame.

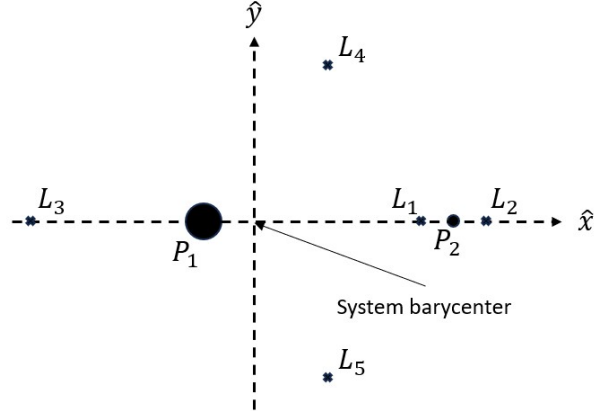


**Figure 2.6.** CR3BP barycentric rotating frame with Lagrange points.

### 2.3.4 Jacobi Constant

One reason that the CR3BP does not have a closed-form analytical solution like the 2BP is there are not enough integrals of the motion, at least that have been discovered to date. However, there is one such constant of the motion in the rotating frame, denoted as the Jacobi constant, and it proves useful as an analogy to energy. The derivation is as follows[5]:

$$\nabla U \cdot \dot{\vec{\rho}} = \frac{\partial U}{\partial x} \dot{x} + \frac{\partial U}{\partial y} \dot{y} + \frac{\partial U}{\partial z} \dot{z} = (\ddot{x} - 2\dot{y})\dot{x} + (\ddot{y} + 2\dot{x})\dot{y} + \ddot{z}\dot{z}, \quad (2.42)$$

where  $\dot{\vec{\rho}}$  is the rotating velocity vector. The middle of Equation (2.42) is equivalent to the total nondimensional time derivative of the pseudo-potential:

$$\frac{dU}{d\tau} = \ddot{x}\dot{x} + \ddot{y}\dot{y} + \ddot{z}\dot{z}, \quad (2.43)$$

where  $\tau$  is nondimensional time. Integrating and rearranging this equation provides the Jacobi constant as a function of rotating position and velocity:

$$C = 2U - \dot{\rho}^2, \quad (2.44)$$

where  $C$  is the Jacobi constant.

This definition of the Jacobi constant is consistent with the Hamiltonian of the system, which is time-invariant in the CR3BP[6]. Note also that as the Jacobi constant increases, the energy of the trajectory decreases.

## 2.4 Patched Dynamical Models

A variety of methods exist to model the gravitational forces of three (or more) celestial bodies in dynamical systems. While a high-fidelity ephemeris model (HFEM) provides the best accuracy, some models utilize simplifying assumptions to reduce computations and gain more insight into the dynamics of the system while maintaining adequate fidelity. For including all of the bodies in one model, there exist several 4-body problems that differ in layout, coherency, and fidelity. Some of the more prominent options are the Bicircular Restricted 4-Body Problem (BCR4BP)[7], Hills Restricted 4-Body Problem (HR4BP)[8], and Quasi-Bicircular Restricted 4-Body Problem (QBCR4BP)[9]. A different approach, and the one used in this investigation, is to patch together 2BP and CR3BP models to build a larger model to represent the dynamics. Two such patched models are outlined here.

### 2.4.1 The Patched 2BP-CR3BP Model

A patched 2BP-CR3BP model is used to describe trajectories as they move between CR3BP systems via a 2BP system. An example from this investigation is leaving the Sun-Earth CR3BP into heliocentric space (modeled as a 2BP) before entering the Sun-Mars CR3BP. While the spacecraft is near a planet, it is modeled in the Sun-planet CR3BP. But once it reaches a specified distance from that planet, it is modeled instead using Keplerian 2BP motion around the Sun[4]. The interface location between the two models is called the

sphere of influence (SoI) since it represents where the gravitational influence of the planet becomes negligible compared to that of the Sun.

Trajectories computed in this model are best represented by using an inertial coordinate frame, centered on the focus of the 2BP, the Sun in this example. In this investigation, trajectories in the 2BP-CR3BP patched model are shown in the Sun-centered Ecliptic J2000 Inertial Frame, as described in Section 2.1.2. Although the Sun-Earth CR3BP is coplanar with this inertial frame, the Sun-Mars CR3BP system is not and Mars is considered to be located at its respective orbital inclination. The  $XY$ -projection of an example 2BP-CR3BP patched model system is shown in Figure 2.7.

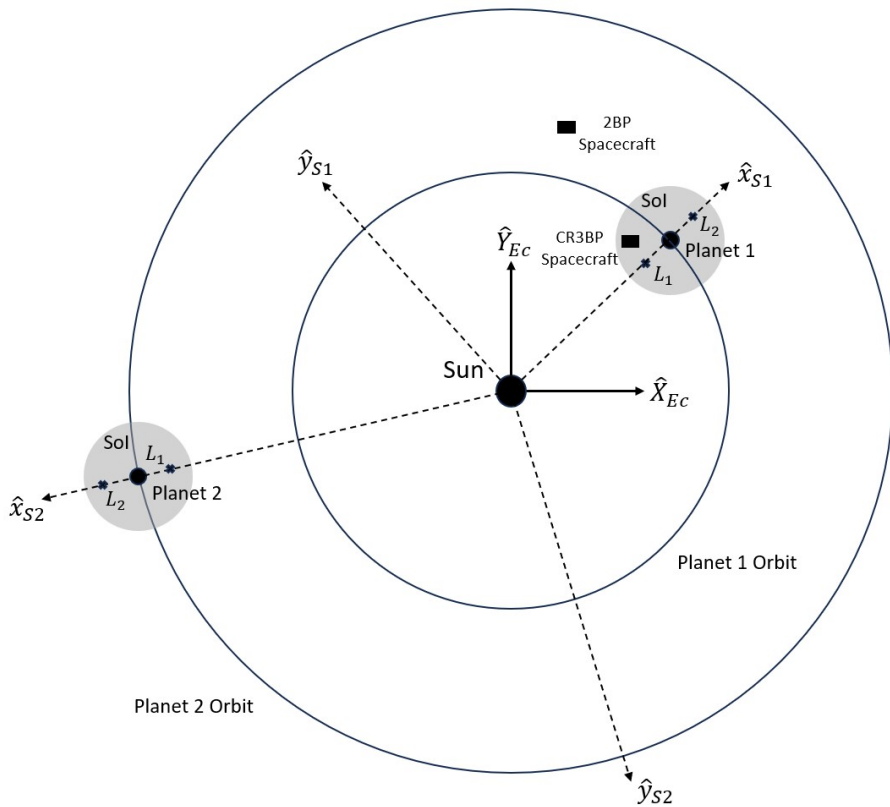


**Figure 2.7.**  $XY$ -Projection of the Patched 2BP-CR3BP Model

The radius of the SoI is a design parameter dependent on the application. For this patched model, an SoI is desired such that CR3BP periodic orbits around the Lagrange points are included. By defining a gravitational ratio:

$$d_{SoI} = \frac{g_2}{g_1}, \quad (2.45)$$

where  $g_i$  is the gravitational acceleration of the respective primary body at a specified location, an SoI radius from the planet can be chosen so that  $d_{SoI}$  is sufficiently small, i.e., the osculating (instantaneous) orbital elements remain near constant in the CR3BP[4].

#### 2.4.2 The Blended CR3BP Model

Two CR3BP models can be blended to form a 4-body model if one of the primary bodies is present in both models. For example, a Sun-Earth CR3BP can be blended with an Earth-Moon CR3BP to form a Sun-Earth-Moon 4-body problem (here, the Earth is the common primary). This method incorporates the difference in inclinations between the two CR3BP models but is now a time-dependent model[10]. Similar to the patched 2BP-CR3BP model, the boundary between the two models is at an SoI, now around the smaller primary of the smaller CR3BP model (the Moon in this example).

Unlike the patched model above, this model is best represented in the barycentric rotating frame of the larger CR3BP model (the Sun-Earth rotating frame in this example). Since the blended model is time-dependent, the portion of the trajectory computed in the smaller CR3BP will be shifted when represented in the larger model depending on the epoch. The  $xy$ -projection of an example blended system is shown in Figure 2.8.

The SoI radius used for the blended model is different from that used for the patched model. As mentioned before, this SoI is centered around the second primary of the smaller system and the gravitational accelerations being compared are the first primary of the larger system and the smaller primary of the second system (e.g., the Sun and the Moon). A blended CR3BP SoI radius is defined as:

$$r_{SoI} = l_{12}^* \left( \frac{m_3}{m_1} \right)^{2/5}, \quad (2.46)$$

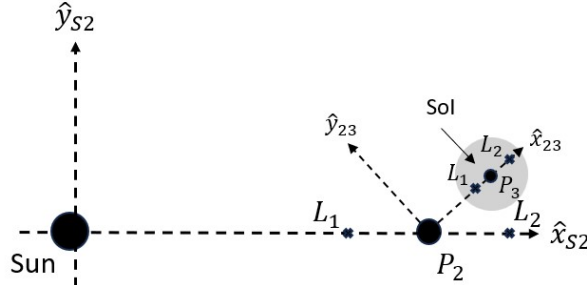


**Figure 2.8.**  $xy$ -Projection of the Blended CR3BP Model

where the primaries are numbered in order of decreasing mass[11].

## 2.5 Coordinate Frame Transformations

Since the patched and blended models used in this investigation use a variety of models centered around different bodies, it is helpful to be able to view any trajectories in multiple reference frames. As mentioned previously, reference frames can be inertial or rotating, and an important component of interplanetary trajectory design is the ability to transform states and trajectories between these two types of frames. A few representative examples of coordinate frame transformations follow.

### 2.5.1 Barycentric Rotating Frame - Primary-Centric Arbitrary Inertial Frame

Most trajectories in a CR3BP are constructed in the barycentric rotating frame where Equation (2.35)-Equation (2.37) are defined (see Figure 2.1). However, it can also be beneficial to view these in an inertial frame centered on one of the primary gravitational bodies. An arbitrary inertial frame can be defined where the inertial unit vectors  $\{\hat{X}, \hat{Y}, \hat{Z}\}$  are equivalent to the rotating unit vectors  $\{\hat{x}, \hat{y}, \hat{z}\}$  at time  $t_0$  (although the frame centers may be in different locations).

The following steps will transform (nondimensionalized) states from the barycentric rotating frame to a primary-centric arbitrary inertial frame:

1. Translate the position states from barycentric to primary-centric:

$$\bar{\rho}_{P \rightarrow s/c} = \bar{\rho}_{s/c} - \bar{\rho}_P. \quad (2.47)$$

2. Rotate the states depending on time since  $t_0$

Recall that the mean motion  $n$  of the rotating frame is constant. When nondimensionalized in the CR3BP,  $\tilde{n} = 1$  and therefore the rotation angle is just  $\tau - \tau_0$ . Since the  $\hat{z}$ - and  $\hat{Z}$ -axes coincide for an arbitrary inertial frame, a simple rotation matrix can be used to rotate the position states:

$$\bar{P} = \begin{bmatrix} \cos(\tau - \tau_0) & -\sin(\tau - \tau_0) & 0 \\ \sin(\tau - \tau_0) & \cos(\tau - \tau_0) & 0 \\ 0 & 0 & 1 \end{bmatrix} \bar{\rho} = {}^I C^R \bar{\rho}, \quad (2.48)$$

where  $\bar{\rho}$  is the rotating position and  $\bar{P}$  is the inertial position.

Basic kinematics can be used to compute the velocity in the rotating frame relative to an inertial observer:

$$\frac{{}^I d\bar{\rho}}{d\tau} = \frac{{}^R d\bar{\rho}}{d\tau} + {}^I \bar{\omega}^R \times \bar{\rho} = \dot{\bar{\rho}} + \hat{z} \times \bar{\rho}, \quad (2.49)$$

where  ${}^I \bar{\omega}^R = \tilde{n} \hat{z}$  is the angular velocity relating the two frames. Therefore:

$$\frac{{}^I d\bar{\rho}}{d\tau} = (\dot{x} - y) \hat{x} + (\dot{y} + x) \hat{y} + \dot{z} \hat{z}. \quad (2.50)$$

Using the rotation matrix  ${}^I C^R$  from Equation (2.48), Equation (2.50) can be written in a matrix form and combined with the position rotation to achieve full state rotation:

$$\bar{Q} = \begin{bmatrix} {}^I C^R & \bar{0} \\ {}^I \dot{C}^R & {}^I C^R \end{bmatrix} \bar{q}, \quad (2.51)$$

where  $\bar{q}$  is the rotating state and  $\bar{Q}$  is the inertial state.

3. Dimensionalize the states if desired (see Section 2.3.2).

To transform a primary-centric arbitrary inertial state to a barycentric rotating state, just reverse the above states (nondimensionalizing if necessary) and invert the state rotation matrix.

### 2.5.2 Barycentric Rotating Frame - Ecliptic J2000 Inertial Frame

When designing a trajectory across multiple systems, it is often useful to view each part of the trajectory in a common inertial reference frame. In this investigation, the Earth Ecliptic J2000 inertial frame, introduced in Section 2.1.2 (Figure 2.2), is used as the common frame for interplanetary trajectories.

The transformation between barycentric rotating frame states and a primary-centric Ecliptic J2000 inertial frame states follows a similar process to the arbitrary inertial frame. However, since this frame is defined by a particular epoch (January 1, 2000), the frame rotation is epoch-dependent:

1. To properly compare the rotating frame to the Ecliptic J2000 inertial frame, the location of the second primary in its orbit at each epoch of the trajectory is needed. This is obtained by retrieving the orbital elements of the second primary at a selected initial epoch from SPICE[2]. These orbital elements are then modified to match the CR3BP orbit assumptions ( $a = l^*$  and  $e = 0$ ). Since the mean motion/angular velocity in the CR3Bp is constant at  $\tilde{n} = 1$ :

$$\theta = \tau - \tau_0 + \theta_0, \quad (2.52)$$

where  $\theta_0$  is the true anomaly at the initial epoch  $t = 0$  obtained from SPICE. These updated orbital elements are then used to calculate the full state vector (in dimensional units) of the second primary relative to the first using Equation (2.22)-Equation (2.28).

2. Dimensionalize the trajectory states, times, and angular velocity (see Section 2.3.2).
3. At each time, translate the position states from barycentric to primary-centric using Equation (2.47) (note that dimensional values should be used).

4. Define the instantaneous state rotation matrix using the second primary's Ecliptic J2000 state vector and angular momentum  $\bar{h}$  (Equation (2.6)) at each time:

$$\hat{x} = \frac{\bar{R}_{P_1 \rightarrow P_2}}{|\bar{R}_{P_1 \rightarrow P_2}|}, \quad (2.53)$$

$$\hat{z} = \frac{\bar{h}}{|\bar{h}|}, \quad (2.54)$$

$$\hat{y} = \hat{z} \times \hat{x}, \quad (2.55)$$

$${}^{Ec}C^R = \begin{bmatrix} \hat{x} & \hat{y} & \hat{z} \end{bmatrix}. \quad (2.56)$$

The full state rotation matrix can be found through the same process used in Section 2.5.1, using a dimensional angular velocity:

$${}^{Ec}\dot{C}^R = \begin{bmatrix} n\hat{y} & -n\hat{x} & \bar{0} \end{bmatrix}. \quad (2.57)$$

in Equation (2.51) with dimensional values.

5. Nondimensionalize the states if desired.

States can be transformed from a primary-centric Ecliptic J2000 inertial frame to a barycentric rotating frame by reversing the above steps and inverting the state rotation matrix. This becomes a useful tool when designing interplanetary trajectories using multi-body dynamics.

### 3. CR3BP DYNAMICAL STRUCTURES

As mentioned in the previous chapter, there is no analytical solution to the CR3BP. Instead, trajectories are propagated using numerical methods. Various numerical techniques are applied to find existing dynamical structures in the model, such as periodic orbits and invariant manifolds, and obtain corresponding initial conditions for propagation. These include differential corrections, natural parameter continuation, eigen decomposition, and Poincaré mapping.

#### 3.1 Differential Corrections

Differential corrections are used to compute solutions in targeting problems that satisfy the provided constraints on the initial condition and the trajectory arc. To do so, it is necessary to be able to relate downstream states to the initial condition.

##### 3.1.1 State Transition Matrix

The state transition matrix (STM) relates variations in an initial state,  $\bar{q}_0 = \bar{q}(t_0)$ , to variations in a downstream state  $\bar{q}(t)$ . Starting from a first-order Taylor series expansion about the baseline trajectory arc, the linear variational equation is derived:

$$\partial \dot{\bar{q}}(t) = A(t) \partial \bar{q}(t), \quad (3.1)$$

where  $A(t)$  is the Jacobian matrix for the equations of motion with respect to the state at time  $t$ . A full derivation for the CR3BP  $A(t)$  matrix can be found in Zimovan, but the result is given here[5]:

$$A(t) = \begin{bmatrix} \frac{\partial x}{\partial x_0} & \frac{\partial x}{\partial y_0} & \frac{\partial x}{\partial z_0} & \frac{\partial x}{\partial \dot{x}_0} & \frac{\partial x}{\partial \dot{y}_0} & \frac{\partial x}{\partial \dot{z}_0} \\ \frac{\partial y}{\partial x_0} & \frac{\partial y}{\partial y_0} & \frac{\partial y}{\partial z_0} & \frac{\partial y}{\partial \dot{x}_0} & \frac{\partial y}{\partial \dot{y}_0} & \frac{\partial y}{\partial \dot{z}_0} \\ \frac{\partial z}{\partial x_0} & \frac{\partial z}{\partial y_0} & \frac{\partial z}{\partial z_0} & \frac{\partial z}{\partial \dot{x}_0} & \frac{\partial z}{\partial \dot{y}_0} & \frac{\partial z}{\partial \dot{z}_0} \\ \frac{\partial \dot{x}}{\partial x_0} & \frac{\partial \dot{x}}{\partial y_0} & \frac{\partial \dot{x}}{\partial z_0} & \frac{\partial \dot{x}}{\partial \dot{x}_0} & \frac{\partial \dot{x}}{\partial \dot{y}_0} & \frac{\partial \dot{x}}{\partial \dot{z}_0} \\ \frac{\partial \dot{y}}{\partial x_0} & \frac{\partial \dot{y}}{\partial y_0} & \frac{\partial \dot{y}}{\partial z_0} & \frac{\partial \dot{y}}{\partial \dot{x}_0} & \frac{\partial \dot{y}}{\partial \dot{y}_0} & \frac{\partial \dot{y}}{\partial \dot{z}_0} \\ \frac{\partial \dot{z}}{\partial x_0} & \frac{\partial \dot{z}}{\partial y_0} & \frac{\partial \dot{z}}{\partial z_0} & \frac{\partial \dot{z}}{\partial \dot{x}_0} & \frac{\partial \dot{z}}{\partial \dot{y}_0} & \frac{\partial \dot{z}}{\partial \dot{z}_0} \end{bmatrix} = \begin{bmatrix} 0 & 0 & 0 & 1 & 0 & 0 \\ 0 & 0 & 0 & 0 & 1 & 0 \\ 0 & 0 & 0 & 0 & 0 & 1 \\ \frac{\partial U}{\partial x \partial x} & \frac{\partial U}{\partial x \partial y} & \frac{\partial U}{\partial x \partial z} & 0 & 2n & 0 \\ \frac{\partial U}{\partial y \partial x} & \frac{\partial U}{\partial y \partial y} & \frac{\partial U}{\partial y \partial z} & -2n & 0 & 0 \\ \frac{\partial U}{\partial z \partial x} & \frac{\partial U}{\partial z \partial y} & \frac{\partial U}{\partial z \partial z} & 0 & 0 & 0 \end{bmatrix}, \quad (3.2)$$

$$\frac{\partial U}{\partial x \partial x} = 1 - \frac{1-\mu}{d^3} - \frac{\mu}{r^3} + \frac{3(1-\mu)(x+\mu)^2}{d^5} + \frac{3\mu(x-1+\mu)^2}{r^5}, \quad (3.3)$$

$$\frac{\partial U}{\partial x \partial y} = \frac{\partial U}{\partial y \partial x} = \frac{3(1-\mu)(x+\mu)y}{d^5} + \frac{3\mu(x-1+\mu)y}{r^5}, \quad (3.4)$$

$$\frac{\partial U}{\partial x \partial z} = \frac{\partial U}{\partial z \partial x} = \frac{3(1-\mu)(x+\mu)z}{d^5} + \frac{3\mu(x-1+\mu)z}{r^5}, \quad (3.5)$$

$$\frac{\partial U}{\partial y \partial y} = 1 - \frac{1-\mu}{d^3} - \frac{\mu}{r^3} + \frac{3(1-\mu)y^2}{d^5} + \frac{3\mu y^2}{r^5}, \quad (3.6)$$

$$\frac{\partial U}{\partial y \partial z} = \frac{\partial U}{\partial z \partial y} = \frac{3(1-\mu)yz}{d^5} + \frac{3\mu yz}{r^5}, \quad (3.7)$$

$$\frac{\partial U}{\partial z \partial z} = -\frac{1-\mu}{d^3} - \frac{\mu}{r^3} + \frac{3(1-\mu)z^2}{d^5} + \frac{3\mu z^2}{r^5}. \quad (3.8)$$

The solution to Equation (3.1):

$$\partial \bar{q}(t) = \frac{\partial \bar{q}(t)}{\partial \bar{q}_0} \partial \bar{q}_0, \quad (3.9)$$

can be rearranged to provide the STM  $\Phi(t, t_0)$ :

$$\Phi(t, t_0) = \frac{\partial \bar{q}(t)}{\partial \bar{q}_0}. \quad (3.10)$$

The equation of motion for the STM can be appended to the CR3BP equations of motion when propagating:

$$\dot{\Phi}(t, t_0) = A(t)\Phi(t, t_0), \quad (3.11)$$

with an initial condition of  $\Phi(t_0, t_0) = I_{6 \times 6}$ .

### 3.1.2 Multi-Variable Newton-Raphson Method

Targeting problems require iterative approaches where an initial guess is updated until it meets a set of constraints to solve a boundary value problem. This investigation uses a multi-variable Newton-Raphson method as a differential corrections process for single-shooting targeting problems, applying analytical or numerical partial derivatives of constraints with respect to the initial conditions.

If  $\bar{X}$  is the free variable vector and  $\bar{F}(\bar{X})$  is the constraint vector, dependent on the free variables, then the goal of the targeting problem is to find  $\bar{X}$  such that  $\bar{F}(\bar{X}) = \bar{0}$  (to a chosen

tolerance). Example free variable and constraint vectors will be introduced in future sections of this chapter and document. Under the Newton-Raphson method, the update equation is again provided by a first-order Taylor series expansion about the initial condition  $\bar{X}_0$ :

$$\bar{F}(\bar{X}) = \bar{F}(\bar{X}_0) + DF(\bar{X}_0)(\bar{X} - \bar{X}_0) = \bar{0}, \quad (3.12)$$

where  $DF(\bar{X})$  is the Jacobian matrix containing the partial derivatives of the constraint vector with respect to the free variable vector.

With this update equation, the next iteration on the initial conditions can be computed. If the number of free variables matches the number of constraints:

$$\bar{X} = \bar{X}_0 - DF(\bar{X}_0)^{-1}\bar{F}(\bar{X}_0), \quad (3.13)$$

and this becomes the new iteration of the initial conditions. Ideally, upon each iteration, the norm of the constraint vector should approach closer to the tolerance. If the number of free variables is greater than the number of constraints, a minimum-norm solution can be used:

$$\bar{X} = \bar{X}_0 - DF(\bar{X}_0)^T(DF(\bar{X}_0)DF(\bar{X}_0)^T)^{-1}\bar{F}(\bar{X}_0). \quad (3.14)$$

When the number of free variables is less than the number of constraints, a least squares solution can be used, but that is not addressed in this investigation.

As a simple targeting example, consider the following planar boundary value problem in Figure 3.1. The objective is to vary the initial velocity and time-of-flight (TOF) to target a desired final position  $\bar{\rho}_d$ . This results in a free variable vector:

$$\bar{X} = \begin{bmatrix} \dot{x}_0 & \dot{y}_0 & \tau \end{bmatrix}^T, \quad (3.15)$$

and constraint vector:

$$\bar{F}(\bar{X}) = \begin{bmatrix} x_f - x_d & y_f - y_d \end{bmatrix}^T = \bar{0}. \quad (3.16)$$

The Jacobian matrix is comprised of the partial derivatives of the constraint vector with respect to the free variable vector, in this case, a combination of the STM and time derivatives:

$$DF(\bar{X}) = \begin{bmatrix} \frac{\partial(x_f - x_d)}{\partial \dot{x}_0} & \frac{\partial(x_f - x_d)}{\partial y_0} & \frac{\partial(x_f - x_d)}{\partial \tau} \\ \frac{\partial(y_f - y_d)}{\partial \dot{x}_0} & \frac{\partial(y_f - y_d)}{\partial y_0} & \frac{\partial(y_f - y_d)}{\partial \tau} \end{bmatrix} = \begin{bmatrix} \phi_{14} & \phi_{15} & \dot{x}_f \\ \phi_{24} & \phi_{25} & \dot{y}_f \end{bmatrix}, \quad (3.17)$$

where  $\phi$  are elements of the STM of the propagated arc. These vectors and the Jacobian matrix can then be used in Equation (3.14) to iteratively solve for the free variable vector that satisfies the constraint vector and solves the provided boundary value problem.

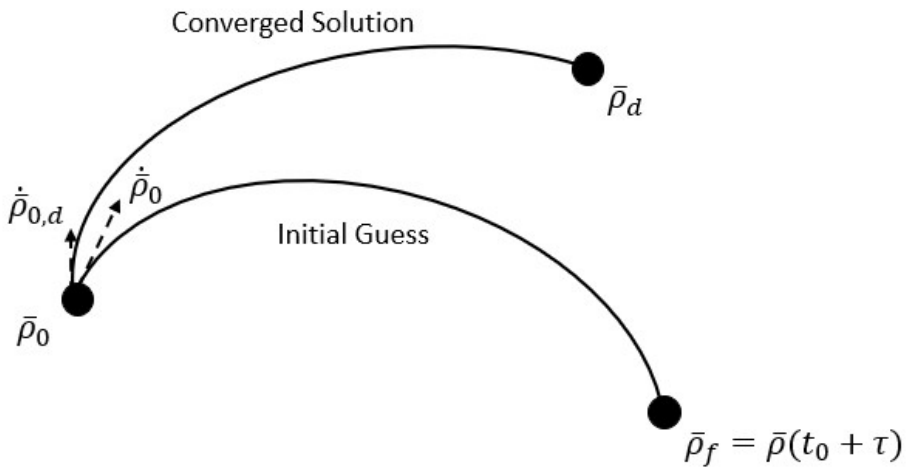


**Figure 3.1.** Simple Targeting Example.

### 3.1.3 Central Difference Method

The Newton-Raphson method uses partial derivatives to solve a targeting problem iteratively. These partial derivatives can be provided analytically (like in the previous example) or numerically using an approximation method such as central differencing. The numerical approach is used in this investigation to check analytical partial derivatives or when the analytical partials are overly complicated.

The central difference method approximates the slope of the solution at discretized points just before and after the initial condition:

$$D\bar{F}_i(\bar{X}_0) = \frac{\partial \bar{F}(\bar{X}_0)}{\partial X_i} = \frac{\bar{F}(X_i + \kappa) - \bar{F}(X_i - \kappa)}{2\kappa}, \quad (3.18)$$

where  $X_i$  is one of the components of the free variable vector and  $\kappa$  is a small perturbation (this investigation uses the square root of the machine tolerance,  $\sqrt{\epsilon}$ ). Each variable in the free variable vector is perturbed in both directions by  $\kappa$ , one at a time, and the constraint vector is evaluated at each new free variable vector and substituted into Equation (3.18) above. Perturbing all of the free variables individually makes up the numerical Jacobian matrix:

$$DF(\bar{X}_0) = \begin{bmatrix} D\bar{F}_1(\bar{X}_0) & \dots & D\bar{F}_m(\bar{X}_0) \end{bmatrix}. \quad (3.19)$$

## 3.2 Periodic Orbits

Using the multi-variable Newton-Raphson scheme described above, periodic solutions can be targeted in a CR3BP system. In the CR3BP, these periodic solutions exist as members of families that share similar geometric characteristics. Some of these orbit families are symmetric about a plane or axis in the rotating frame and this information can be utilized in the targeting process. In addition, the initial conditions for these families can be obtained through a variety of methods including linear variational equations about the Lagrange points and bifurcations from other orbit families. All of the orbit families used in this investigation and shown here were selected for their relative instability in the Earth-Moon CR3BP. For some example initial conditions for these orbit families and others, see NASA Jet Propulsion Laboratory's CR3BP orbit database[12].

### 3.2.1 Lyapunov Orbits

#### A Lyapunov Targeter

To demonstrate the periodic orbit targeting process, the Newton-Raphson scheme will be used to solve for a periodic orbit in the  $xy$ -plane of the rotating frame around the first

Lagrange point. This family of solutions is known as the  $L_1$  Lyapunov family and they are symmetric about the  $xz$ -plane. Therefore, instead of targeting the full orbit, it is only necessary to target half of it, from one perpendicular crossing of the  $xz$ -plane to the next. To target one of these orbits at a specified energy level (Jacobi constant), consider the free variable vector:

$$\bar{X} = \begin{bmatrix} x_0 & \dot{y}_0 & \tau \end{bmatrix}^T. \quad (3.20)$$

Since the boundary value problem being solved starts from a perpendicular crossing, it is only necessary to allow  $x_0$  and  $\dot{y}_0$  to vary as the rest of the initial states will all be 0. In Equation (3.20),  $\tau$  represents the nondimensional propagation time (TOF) of the initial conditions. To target another perpendicular crossing for the endpoint of the trajectory arc, the following constraint vector is used:

$$\bar{F}(\bar{X}) = \begin{bmatrix} y_f & \dot{x}_f & C - C_d \end{bmatrix}^T = \bar{0}, \quad (3.21)$$

where  $C$  is the Jacobi constant of the propagated arc and  $C_d$  is the desired Jacobi constant. The Jacobian matrix is then comprised of partial derivatives from the STM, time derivatives, and partial derivatives of the Jacobi constant with respect to state variables:

$$DF(\bar{X}) = \begin{bmatrix} \frac{\partial y_f}{\partial x_0} & \frac{\partial y_f}{\partial \dot{y}_0} & \frac{\partial y_f}{\partial \tau} \\ \frac{\partial \dot{x}_f}{\partial x_0} & \frac{\partial \dot{x}_f}{\partial \dot{y}_0} & \frac{\partial \dot{x}_f}{\partial \tau} \\ \frac{\partial(C-C_d)}{\partial x_0} & \frac{\partial(C-C_d)}{\partial \dot{y}_0} & \frac{\partial(C-C_d)}{\partial \tau} \end{bmatrix} = \begin{bmatrix} \phi_{21} & \phi_{25} & \dot{y}_f \\ \phi_{41} & \phi_{45} & \ddot{x}_f \\ 2x_0 - \frac{2(x_0+\mu)(1-\mu)}{d^3} - \frac{2\mu(x_0-1+\mu)}{r^3} & -2\dot{y}_0 & 0 \end{bmatrix}. \quad (3.22)$$

This Jacobian matrix can then be used with Equation (3.13) to iteratively solve for the free variable vector  $\bar{X}$  that solves the provided problem. This provides the initial state and half of the propagation time for a periodic Lyapunov orbit.

## Lyapunov Initial Guess

An initial guess for a Lyapunov orbit close to the Lagrange point can come from variational equations of motion, linearized about the equilibrium point:

$$x_0 = x_L + \xi, \quad (3.23)$$

$$\dot{y}_0 = -\beta_3 \xi s, \quad (3.24)$$

where  $\xi$  is a chosen variation from the  $x$ -value of the Lagrange point,

$$\beta_1 = 2 - \frac{\frac{\partial U}{\partial x \partial x} + \frac{\partial U}{\partial y \partial y}}{2}, \quad (3.25)$$

$$\beta_2 = \sqrt{-\frac{\partial U}{\partial x \partial x} \frac{\partial U}{\partial y \partial y}}, \quad (3.26)$$

$$s = \sqrt{\beta_1 + \sqrt{\beta_1^2 + \beta_2^2}}, \quad (3.27)$$

$$\beta_3 = \frac{s^2 + \frac{\partial U}{\partial x \partial x}}{2s}. \quad (3.28)$$

The last part of the initial guess for the free variable vector is the half-period of the orbit  $\tau$ . This can be approximated by propagating the initial state guess until it reaches the  $x$ -axis.

### Converged Lyapunov Orbit

The linear variational equations only approximate the dynamics very close to the Lagrange point. Using  $\xi = 0.005$  as the initial variation in the  $x$ -direction from the  $L_1$  Lagrange point in the Earth-Moon system:

$$\bar{X}_0 = \begin{bmatrix} 0.841915 & -0.0418614 & 1.29755 \end{bmatrix}^T, \quad (3.29)$$

and from the guess for the initial state,  $C_d = 3.186877$ . This initial free variable guess is propagated using the CR3BP equations of motion and is represented by the dashed curve in Figure 3.2. After targeting a perpendicular crossing using the targeter described above, the solution can be propagated (for  $2\tau$ ) to obtain the full periodic Lyapunov orbit, shown as a closed, solid curve in Figure 3.2. Note that while the energy of the converged solution matches that of the initial guess, the  $x$ - and  $y$ -values have shifted slightly.

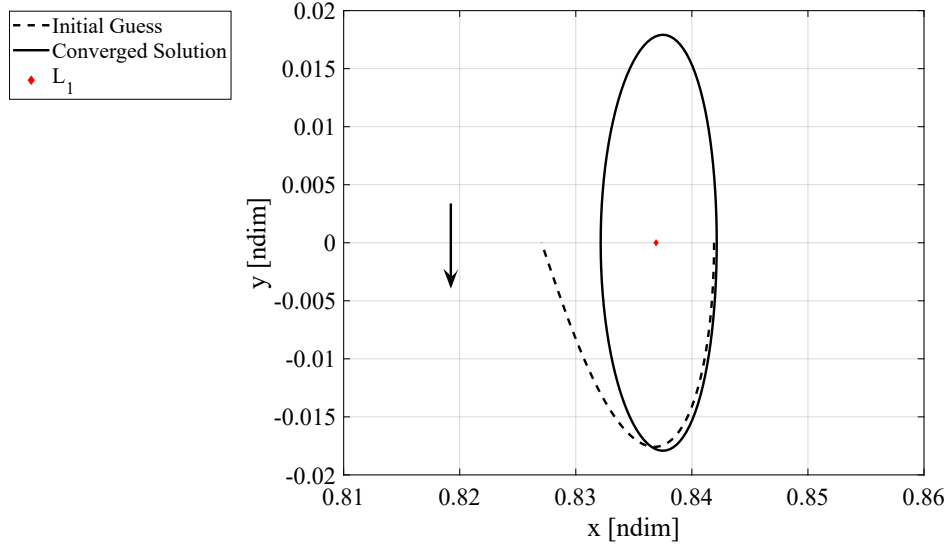


**Figure 3.2.** Converged periodic Lyapunov orbit in the Earth-Moon barycentric rotating frame.

### Natural Parameter Continuation

The process described above produces a single solution near the Lagrange point. To compute more solutions (orbits) in the family, especially further away from the Lagrange point where the linear variational equations no longer apply, converged solutions can be used in a continuation scheme to find other family members. This investigation utilizes natural parameter continuation, where one of the parameters of a converged solution is changed by a small amount. This new guess for an orbit is then converged, and a new solution is obtained. This continuation process can then be repeated until the scheme reaches a natural/dynamical end or a desired orbit is reached. Natural parameters of the orbit include (but are not limited to) components of the initial state, the period, or the Jacobi constant. Figure 3.3 shows a large portion of the  $L_1$  Lyapunov family in the Earth-Moon system, continued in Jacobi constant from the orbit in Figure 3.2. Lyapunov families also exist about  $L_2$  and  $L_3$  and can be computed via the same process. Since  $L_2$  Lyapunovs are also used in this investigation, they are shown in Figure 3.4.

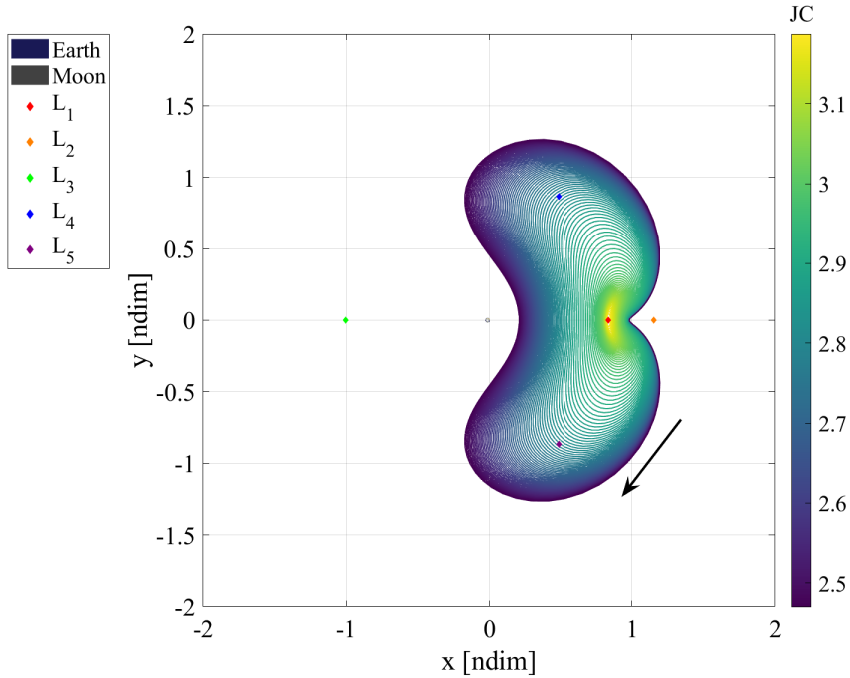


**Figure 3.3.** Earth-Moon  $L_1$  Lyapunov orbit family.

### 3.2.2 Orbital Stability

Before discussing other orbit families, it is important to introduce orbital stability as it leads to orbit family bifurcations and another way to generate new orbit families. Orbital stability helps describe the characteristics of the orbit and the surrounding dynamics. The stability of an orbit also determines the best transfer design strategies to minimize the  $\Delta v$  cost.

### Monodromy Matrix

The STM of one revolution of a periodic orbit in the CR3BP,  $\Phi(t_0 + \mathbb{P}, t_0)$ , is called the monodromy matrix, and discretely maps the linear growth of perturbations. Some useful properties of the monodromy matrix are that it is symplectic, it has a determinant of 1, and its eigenvalues occur in reciprocal pairs[13]. Since the trajectory is periodic, two of the eigenvalues (one pair) are always 1, denoted the trivial pair, and correspond to the trajectory's periodicity and membership in a family of solutions.

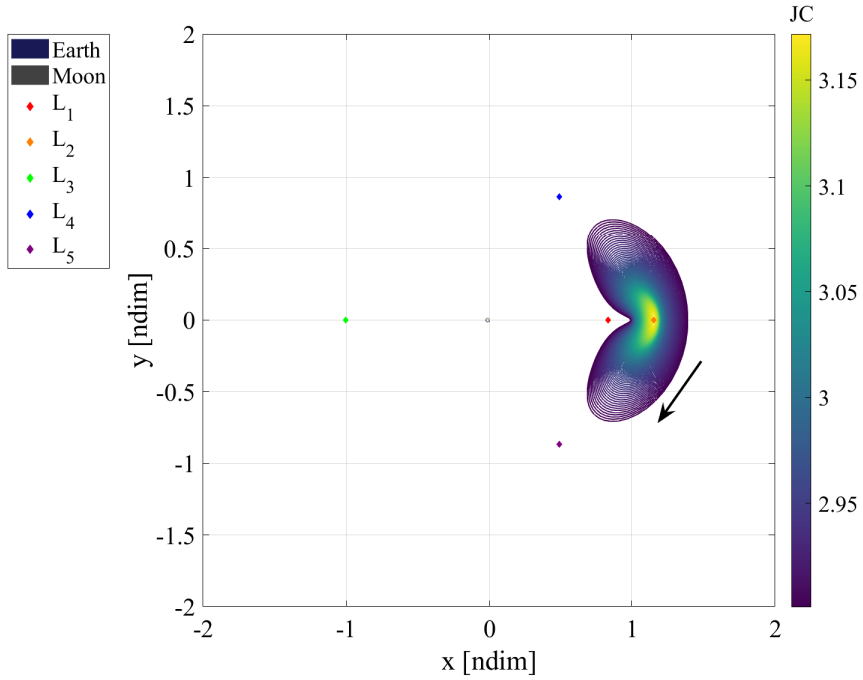


**Figure 3.4.** Earth-Moon  $L_2$  Lyapunov orbit family.

The stability of the orbit is characterized by the remaining two pairs of eigenvalues. Since the monodromy matrix is a discrete-time mapping, eigenvalues that lie within the unit circle (magnitude less than 1) in the complex plane are stable and those outside the unit circle are unstable. Perturbations in the stable subspace will flow back toward the orbit, while perturbations in the unstable subspace will depart the orbit. If the eigenvalues lie directly on the unit circle, then the corresponding flow is in the center subspace and remains bounded around the orbit. When the stability of an eigenvalue pair changes, it can indicate a change in the characteristics of orbits within a family and sometimes leads to a bifurcation in the family, discussed later.

The overall stability of the orbit is then determined by all of the eigenvalues of its monodromy matrix. If any of the eigenvalues are unstable (greater than 1), then the orbit is considered linearly unstable. Note that the existence of an unstable eigenvalue implies the existence of a stable eigenvalue because of the reciprocal pairs. Otherwise, the orbit is considered marginally stable and all of the eigenvalues reside on the unit circle. Throughout

an orbit family, while the stability of the members may change, the eigenvalues experience a smooth (but not necessarily monotonic) evolution.

## Stability Index

A variety of metrics exist to more succinctly portray the stability of orbits, rather than viewing all of the eigenvalues. One such metric is a stability index, of which there are a variety of definitions whose usefulness vary depending on the application. In this investigation, the focus is on just the overall stability of the orbit — whether it is unstable or marginally stable — so a metric that can quickly differentiate between these behaviors suffices. Therefore, the following definition is used[14]:

$$\varsigma = \|\bar{\lambda}\|_\infty, \quad (3.30)$$

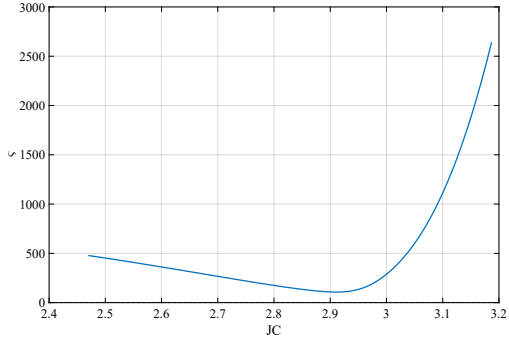
where  $\bar{\lambda}$  is a vector of the eigenvalues of the monodromy matrix and the infinity norm returns the magnitude of the largest (magnitude) element of the vector. With this definition,  $\varsigma > 1$  indicates an unstable orbit and  $\varsigma = 1$  indicates one that is marginally stable. Other definitions can be found in Zimovan Spreen's work[13].

Like the eigenvalues themselves, the evolution of the stability index over an orbit family is smooth. Figure 3.5 shows the stability indices for the members of the  $L_1$  (a) and  $L_2$  (b) Lyapunov families from Figure 3.3 and Figure 3.4. A larger stability index means that the orbit has a higher instability and perturbations will experience faster growth. Note that all of the members of both of these families are unstable. However, there are stability changes among individual eigenvalues within each family that can lead to bifurcations.

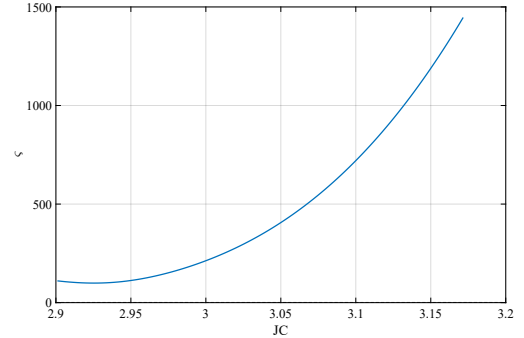
## Time Constant

Another useful metric of stability is the time constant, which approximates how long it takes, in time units or in orbit revolutions, for a perturbation to grow by a factor of e:

$$\Upsilon = \frac{1}{\ln \varsigma}, \quad (3.31)$$



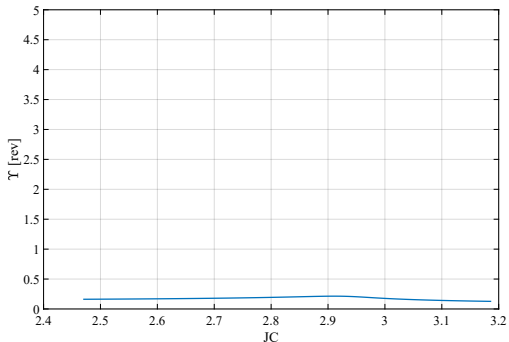
(a)  $L_1$



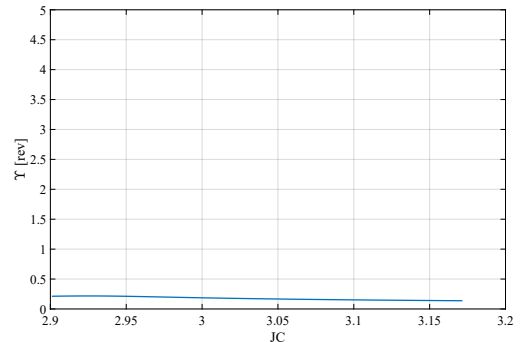
(b)  $L_2$

**Figure 3.5.** Earth-Moon Lyapunov family stability index evolution.

where the dimensions are orbit revolutions. This equation can be multiplied by the period of the orbit  $\mathbb{P}$  to produce the time constant in time units. Figure 3.6 shows the time constant evolution of both Lyapunov families in orbit revolutions. Note that a larger time constant indicates that it takes longer for a perturbation, meaning that the orbit is less unstable, and a marginally stable orbit has an infinite time constant.



(a)  $L_1$



(b)  $L_2$

**Figure 3.6.** Earth-Moon Lyapunov family time constant evolution.

## Bifurcations

Within the context of the CR3BP, bifurcation theory can be used to detect changes in orbit stability characteristics within a family that can sometimes lead to the generation of orbit families that branch off from the original family. Zimovan Spreen provides a more thorough

analysis of how bifurcation theory can be applied to the CR3BP so only the information most relevant to this investigation will be provided here[13].

Two main bifurcation types are relevant to the orbits used in this analysis:

- **Tangent bifurcations** occur when an eigenvalue pair goes to 1, either from the unit circle or the real axis. With a cyclic fold tangent bifurcation, which occurs at an extremum in the Jacobi constant, the stability of the eigenvalues changes, but there is no new family of solutions created. Pitchfork tangent bifurcations produce two new families that have the same stability as the original family. The last subtype, transcritical tangent bifurcations, produce a new family and a change in the eigenvalue stability of the original family.
- **Period-multiplying bifurcations** occur when an eigenvalue pair reaches a root of 1 ( $\sqrt{1}$ ,  $\sqrt[3]{1}$ ,  $\sqrt[m]{1}$ , etc.). In general, this produces a new family with a period of  $m$  times the original, but not necessarily a change in stability. The most commonly seen subtype is the period-doubling bifurcation, where the pair of eigenvalues meets at  $-1$ , either from the unit circle or the real axis. This results in a change in the stability of the eigenvalues and a new family that has double the period of the original family.

There are other methods of detecting bifurcations beyond examining the evolution of the eigenvalues such as Broucke stability or bifurcation diagrams that are also described in Zimovan Spreen[13].

## New Family Generation from Bifurcation

To find the initial conditions for an orbit in a new family from a bifurcation, first, the precise bifurcating orbit (within a tolerance) must be obtained. This can be done through a simple bisection algorithm. The Jacobian matrix of this bifurcating orbit should have an additional nullspace compared to the other orbits in the family since another pair of eigenvalues (besides the trivial pair) is at 1. Note that for a period-multiplying bifurcation, the orbit must be propagated for  $m$  revolutions to obtain the proper Jacobian matrix. When

this is the case, one of the nullspace vectors points in the direction of continuing the old family, while the other vector indicates a direction for the new family.

Using a singular value decomposition (SVD), this new nullspace direction can be identified by the right singular vector of  $DF$  that corresponds to the additional nullspace. Stepping in this direction from the bifurcating orbit's initial conditions and correcting for a periodic solution should result in a new periodic orbit belonging to the new family. This approach is also known as pseudo-arc length continuation and the new member can then be continued using any scheme to obtain the new family.

### 3.2.3 Halo Orbits

#### A Halo Targeter

Similar to Lyapunov orbits, halo orbits are symmetric about the  $xz$ -plane although they are spatial in the rotating frame and not limited to the  $xy$ -plane. This again allows for targeting only half of the periodic orbit, from one perpendicular crossing to the next. Since there is now a  $z$ -component to the orbits, it is helpful to introduce a new free variable and constraint for the halo targeter:

$$\bar{X} = \begin{bmatrix} x_0 & z_0 & \dot{y}_0 & \tau \end{bmatrix}^T, \quad (3.32)$$

$$\bar{F}(\bar{X}) = \begin{bmatrix} y_f & \dot{x}_f & \dot{z}_f & C - C_d \end{bmatrix}^T = \bar{0}, \quad (3.33)$$

$$DF(\bar{X}) = \begin{bmatrix} \phi_{21} & \phi_{23} & \phi_{25} & \dot{y}_f \\ \phi_{41} & \phi_{43} & \phi_{45} & \ddot{x}_f \\ \phi_{61} & \phi_{63} & \phi_{65} & \ddot{z}_f \\ 2x_0 - \frac{2(x_0+\mu)(1-\mu)}{d^3} - \frac{2\mu(x_0-1+\mu)}{r^3} & -\frac{2z_0(1-\mu)}{d^3} - \frac{2z_0\mu}{r^3} & -2\dot{y}_0 & 0 \end{bmatrix}. \quad (3.34)$$

The result of this targeting will provide the initial state ( $y_0 = \dot{x}_0 = \dot{z}_0 = 0$ ) and half of the propagation time for a periodic halo orbit.

## Converged Halo Families

The initial guess for a halo orbit comes from a bifurcating orbit in a Lyapunov family. At  $C \approx 3.174352$ , the  $L_1$  Lyapunov family has a tangent bifurcation and the  $L_1$  halo family is formed. The pseudo-arc length method for generating an initial guess can be used as described above to obtain the initial guess for the initial state, propagation time, and Jacobi constant. Using natural parameter continuation, more of the family is produced, shown in Figure 3.7. Since the Lyapunov orbit can bifurcate above or below the  $xy$ -plane, two halves of the family are formed. Figure 3.7 is denoted the  $L_1$  southern halos because most of the orbit is spent south (in the rotating frame) of the Moon.

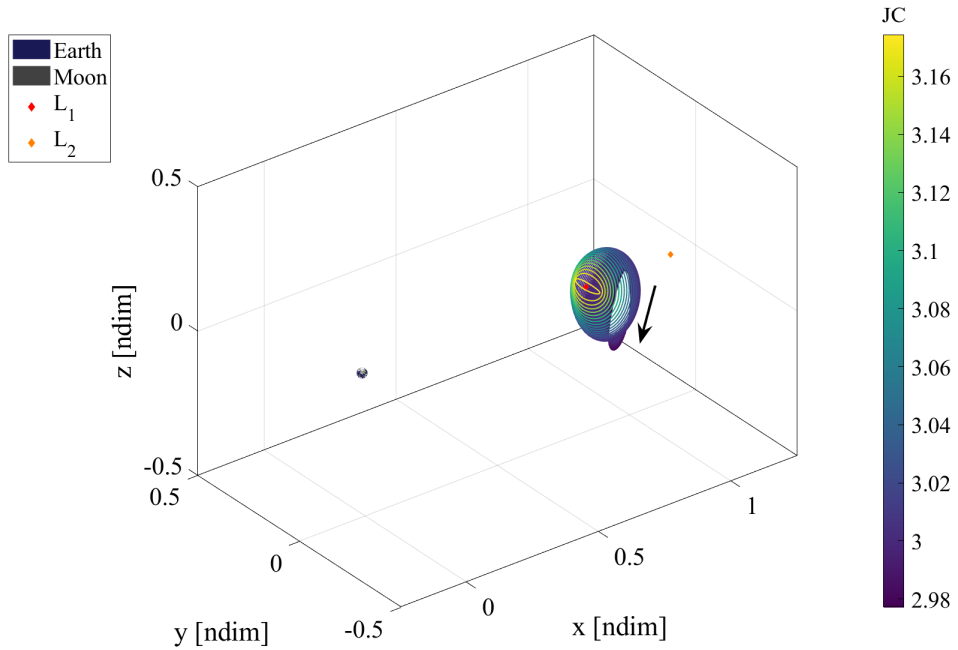


**Figure 3.7.** Earth-Moon  $L_1$  southern halo orbit family.

Figure 3.8 shows the  $L_2$  southern halo family, generated in the same way as the  $L_1$  halos but from the  $L_2$  Lyapunov family. Note that these halo families are not monotonic in Jacobi constant. The stability indices for both families are shown in Figure 3.9.  $L_3$  halos also exist, but are not used in this investigation.

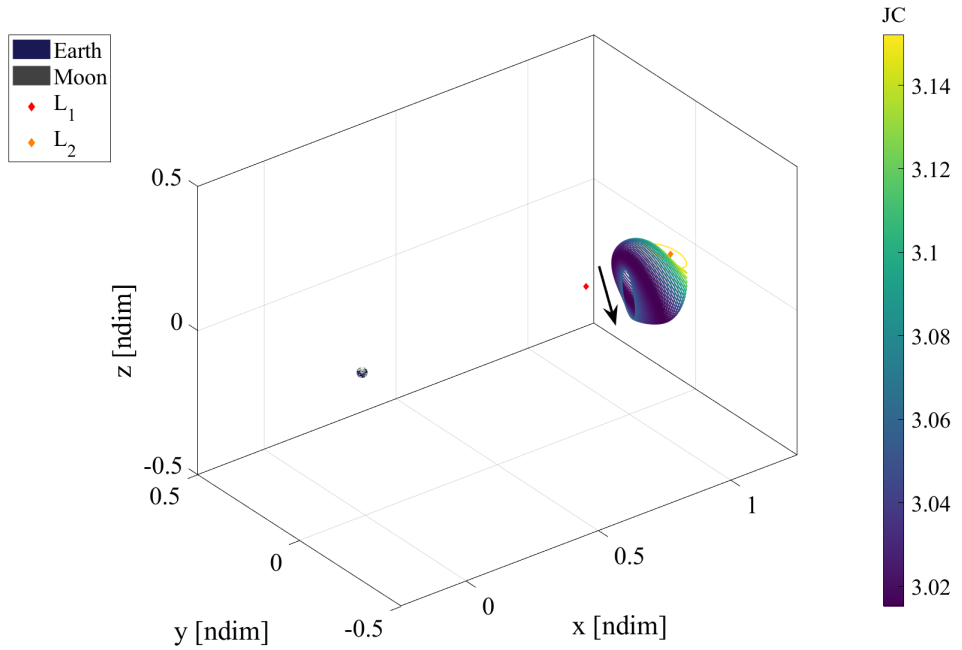


**Figure 3.8.** Earth-Moon  $L_2$  southern halo orbit family.

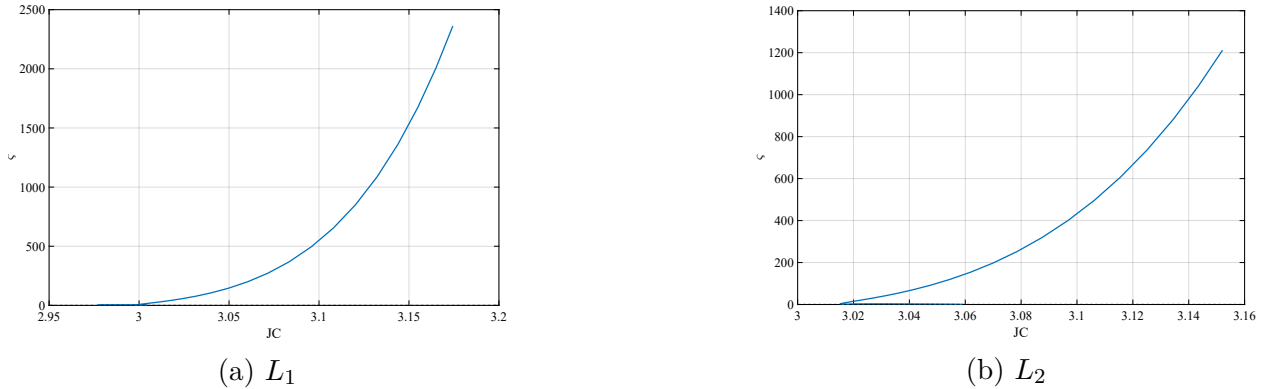


**Figure 3.9.** Earth-Moon Halo family stability index evolution.

### 3.2.4 Butterfly Orbits

Butterfly orbits is another name for the  $P_2HO_1$   $L_2$  orbit family: the period-doubling bifurcation from the  $L_2$  halo family with the smallest perilune[13]. Conveniently, the same targeter can be used for this family as with the halos above. The same pseudo-arc length method can also be used to obtain the initial guess from the bifurcating halo, remembering

to double the period of the orbit first. A portion of this family is shown in Figure 3.10 and the stability indices are shown in Figure 3.11.

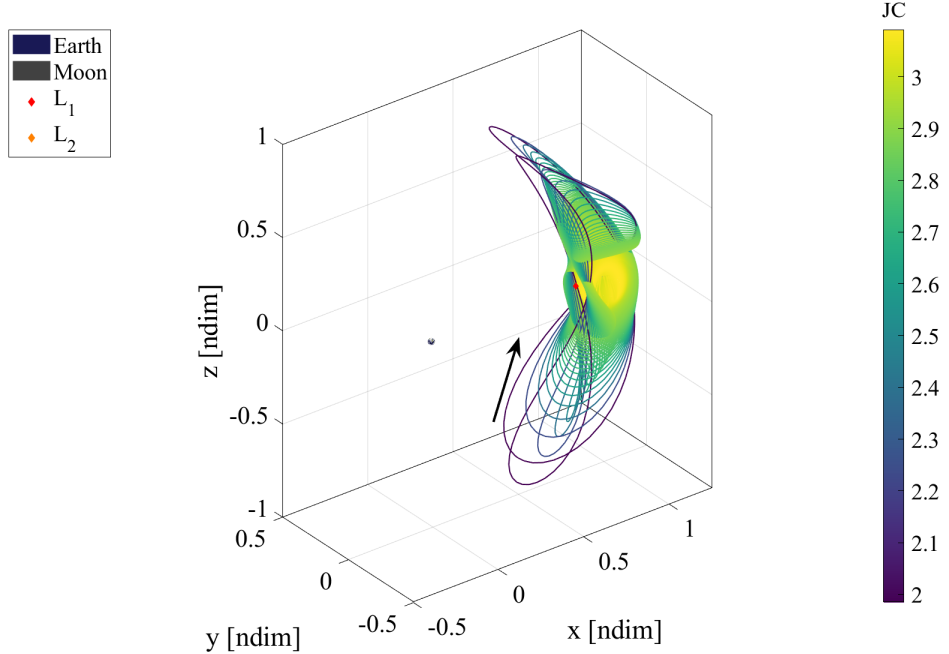


**Figure 3.10.** Earth-Moon butterfly family.

### 3.2.5 Axial Orbits

#### An Axial Targeter

Another spatial orbit family, the axial orbits, comes from a different tangent bifurcation in the Lyapunov families. These orbits have symmetry only about the  $x$ -axis; therefore, the perpendicular crossings must lie on the  $x$ -axis, unlike the halo orbits:

$$\bar{X} = \begin{bmatrix} x_0 & \dot{y}_0 & \dot{z}_0 & \tau \end{bmatrix}^T, \quad (3.35)$$

$$\bar{F}(\bar{X}) = \begin{bmatrix} y_f & z_f & \dot{x}_f & C - C_d \end{bmatrix}^T = \bar{0}, \quad (3.36)$$

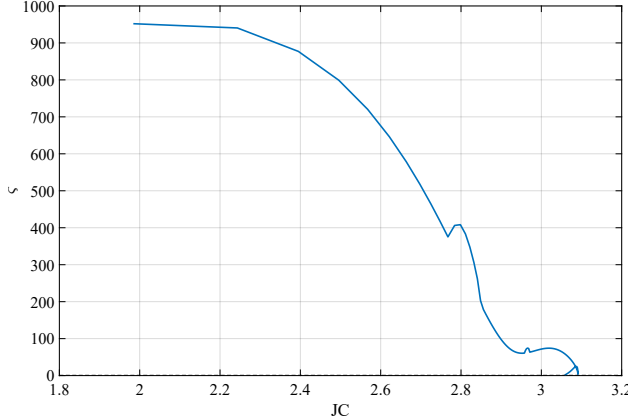


**Figure 3.11.** Earth-Moon butterfly family stability index evolution.

$$DF(\bar{X}) = \begin{bmatrix} \phi_{21} & \phi_{25} & \phi_{26} & \dot{y}_f \\ \phi_{31} & \phi_{35} & \phi_{36} & \dot{z}_f \\ \phi_{41} & \phi_{45} & \phi_{46} & \ddot{x}_f \\ 2x_0 - \frac{2(x_0 + \mu)(1 - \mu)}{d^3} - \frac{2\mu(x_0 - 1 + \mu)}{r^3} & -2\dot{y}_0 & -2\dot{z}_0 & 0 \end{bmatrix}. \quad (3.37)$$

The result of this targeting will provide the initial state ( $y_0 = z_0 = \dot{x}_0 = 0$ ) and half of the propagation time for a periodic axial orbit.

## Converged Axial Families

From the methods used to obtain the halo families, the  $L_1$  and  $L_2$  axial families can also be obtained, shown in Figure 3.12 and Figure 3.13 respectively. Similar to the halo orbits, two halves to the family can be obtained by bifurcating above or below the  $xy$ -plane, making these the  $L_1$  northeast and  $L_2$  northwest axial families. Their stability indices follow in Figure 3.14. Again, there is an  $L_3$  axial family, but it is not used in this investigation.

### 3.2.6 Vertical Orbits

#### A Vertical Targeter

Vertical orbits benefit from double symmetry about both the  $xz$ - and  $xy$ -planes. This allows for targeting only a quarter of the orbit, with a perpendicular crossing of the  $xz$ -plane

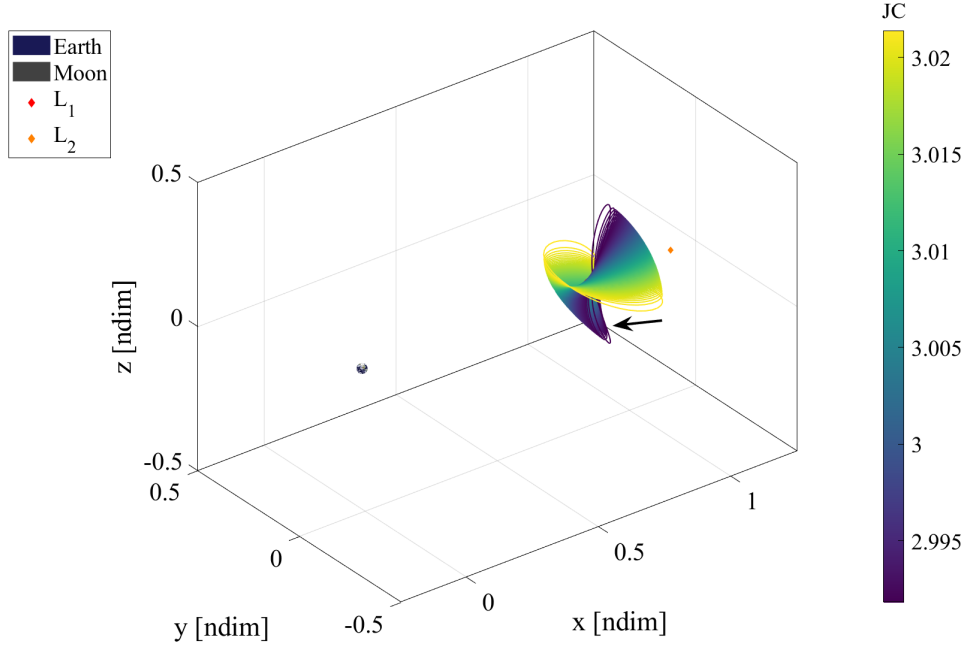


**Figure 3.12.** Earth-Moon  $L_1$  northeast axial orbit family.

on one end of the arc and a perpendicular crossing of the  $x$ -axis on the other. Starting from the  $xz$ -plane crossing:

$$\bar{X} = \begin{bmatrix} x_0 & z_0 & \dot{y}_0 & \tau \end{bmatrix}^T, \quad (3.38)$$

$$\bar{F}(\bar{X}) = \begin{bmatrix} y_f & z_f & \dot{x}_f & C - C_d \end{bmatrix}^T = \bar{0}, \quad (3.39)$$

$$DF(\bar{X}) = \begin{bmatrix} \phi_{21} & \phi_{23} & \phi_{25} & \dot{y}_f \\ \phi_{31} & \phi_{33} & \phi_{35} & \dot{z}_f \\ \phi_{41} & \phi_{43} & \phi_{45} & \ddot{x}_f \\ 2x_0 - \frac{2(x_0 + \mu)(1 - \mu)}{d^3} - \frac{2\mu(x_0 - 1 + \mu)}{r^3} & -\frac{2z_0(1 - \mu)}{d^3} - \frac{2z_0\mu}{r^3} & -2\dot{y}_0 & 0 \end{bmatrix}. \quad (3.40)$$

The result of this targeting will provide the initial state ( $y_0 = \dot{x}_0 = \dot{z}_0 = 0$ ) at the perpendicular crossing of the  $xz$ -plane (top/bottom of the orbit) and one-quarter of the propagation time for a periodic vertical orbit.

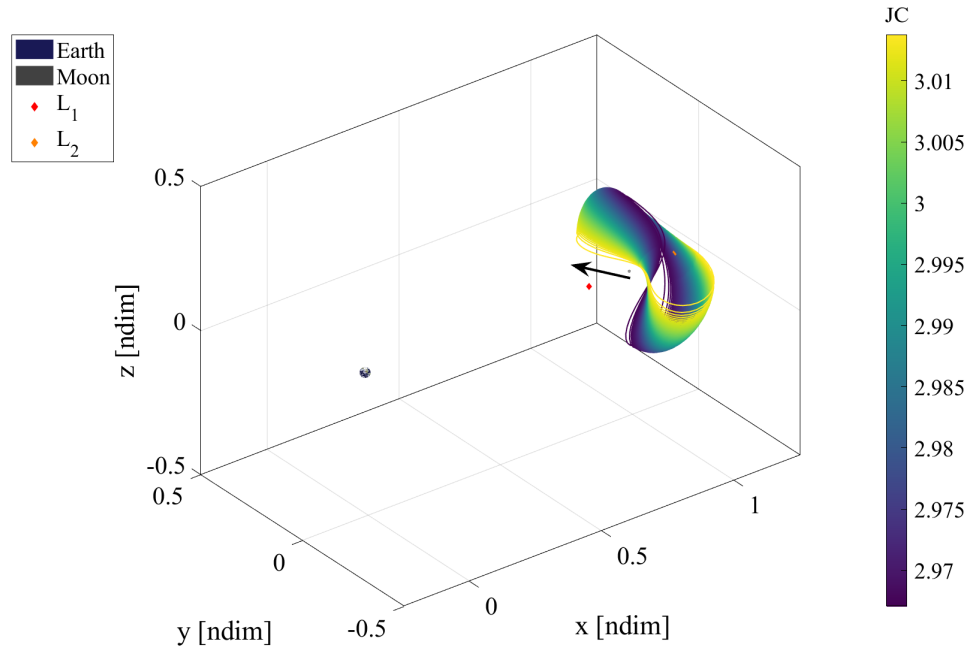


**Figure 3.13.** Earth-Moon  $L_2$  northwest axial orbit family.

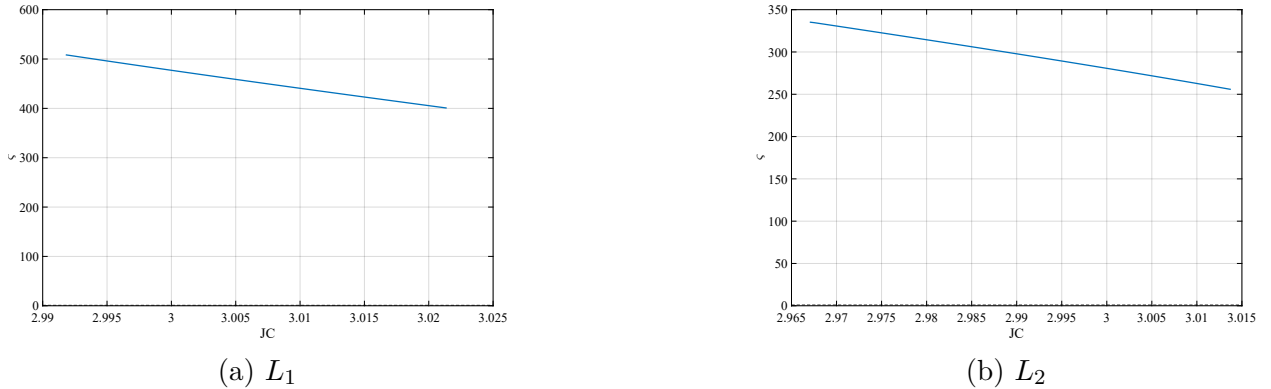


**Figure 3.14.** Earth-Moon axial family stability index evolution.

### Converged Vertical Families

The vertical orbit family bifurcates from the end of the axial family when the axial orbit intersects itself and resembles a figure-eight. Stepping in one direction shrinks the orbits as the family collapses down to its origin Lagrange point. The other direction expands the orbits until they look like clam shells, demonstrated for the  $L_1$  family in Figure 3.15. Similar

behavior occurs with the  $L_2$  vertical family in Figure 3.16. Figure 3.17 shows the stability indices for these two families;  $L_3$  verticals are not used in this investigation.

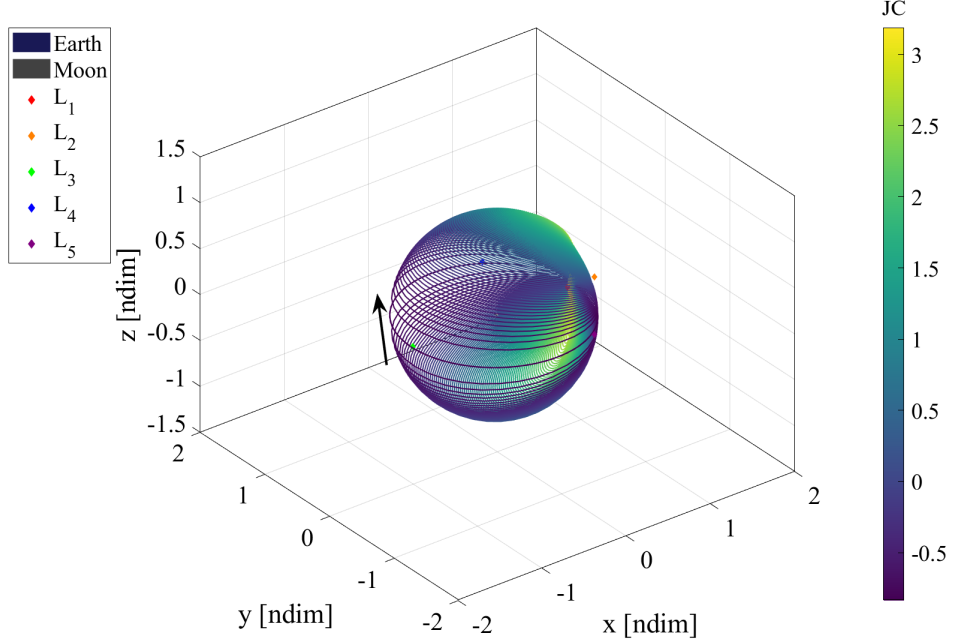


**Figure 3.15.** Earth-Moon  $L_1$  vertical orbit family.

### 3.2.7 Equilateral Long Period Orbits

#### A Planar Equilateral Orbit Targeter

Similar to the Lyapunov orbits around the colinear equilibrium points, there are planar orbits around the equilateral equilibrium points  $L_4$  and  $L_5$ ; however, they do not have symmetry that can be exploited. Therefore, the full period of the orbit needs to be targeted, constraining periodicity between the propagation start and end points. Note that since the Jacobi constant of a propagated trajectory is naturally constrained, constraining periodicity only requires constraining five out of the six states (three out of the four for a planar problem):

$$\bar{X} = \begin{bmatrix} x_0 & \dot{x}_0 & \dot{y}_0 & \tau \end{bmatrix}^T, \quad (3.41)$$

$$\bar{F}(\bar{X}) = \begin{bmatrix} x_f - x_0 & y_f - y_0 & \dot{x}_f - \dot{x}_0 & C - C_d \end{bmatrix}^T = \bar{0}, \quad (3.42)$$

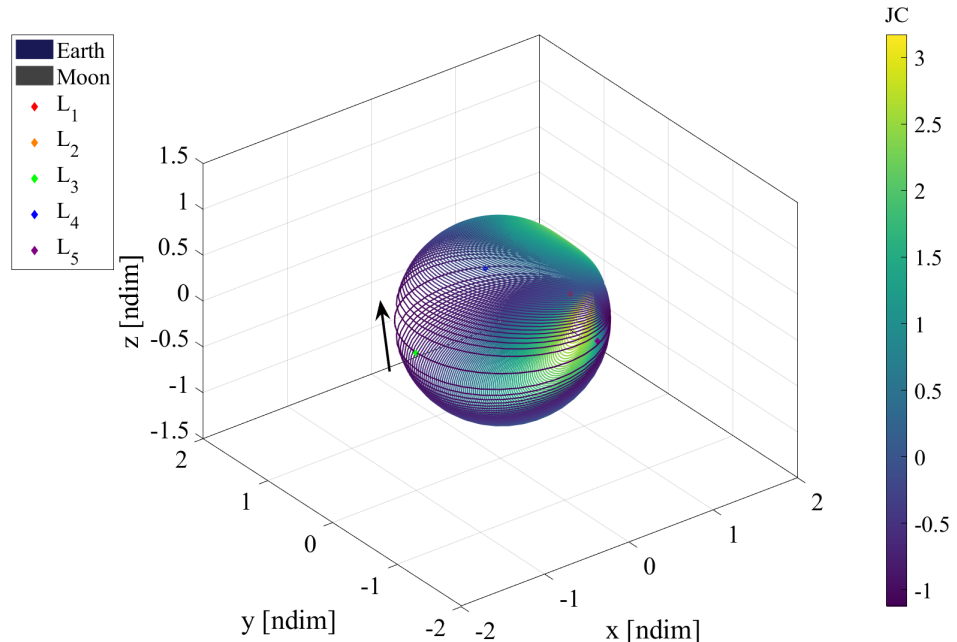


**Figure 3.16.** Earth-Moon  $L_2$  vertical orbit family.

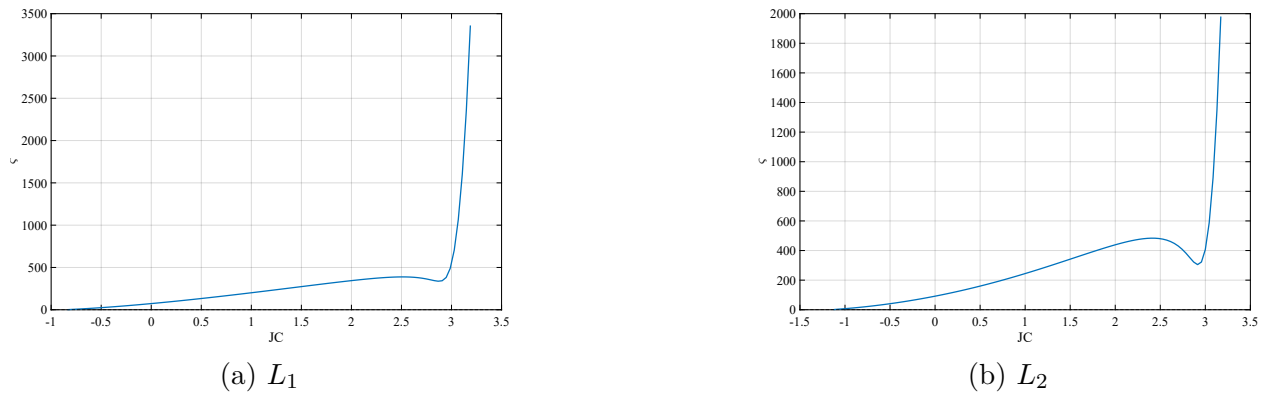


**Figure 3.17.** Earth-Moon vertical family stability index evolution.

$$DF(\bar{X}) = \begin{bmatrix} \phi_{11} - 1 & \phi_{14} & \phi_{15} & \dot{x}_f \\ \phi_{21} & \phi_{24} & \phi_{25} & \dot{y}_f \\ \phi_{41} & \phi_{44} - 1 & \phi_{45} & \ddot{x}_f \\ 2x_0 - \frac{2(x_0 + \mu)(1 - \mu)}{d^3} - \frac{2\mu(x_0 - 1 + \mu)}{r^3} & -2\dot{x}_0 & -2\dot{y}_0 & 0 \end{bmatrix}. \quad (3.43)$$

Since  $z = \dot{z} = 0$ , this targeter provides five of the six initial state variables and the full period for the planar equilateral orbit.

## Equilateral Long Period Orbit Initial Guess

Initial guesses for the planar equilateral orbits close to the Lagrange point can come from linear variational equations of motion about the equilibrium point:

$$x_0 = x_L + \xi, \quad (3.44)$$

$$y_0 = y_L + \eta, \quad (3.45)$$

$$\dot{x}_0 = \alpha s, \quad (3.46)$$

$$\dot{y}_0 = \beta s, \quad (3.47)$$

where  $\xi$  and  $\eta$  are chosen variations from the Lagrange point,

$$s = \text{Im}(\lambda), \quad (3.48)$$

$$\alpha = \frac{\xi \frac{\partial U}{\partial x \partial y} + \eta \left( \frac{\partial u}{\partial y \partial y} + s^2 \right)}{2s}, \quad (3.49)$$

$$\beta = -\frac{\xi \left( \frac{\partial U}{\partial x \partial x} + s^2 \right) + \eta \frac{\partial U}{\partial x \partial y}}{2s}. \quad (3.50)$$

The linearization has two frequencies, short and long, and the choice of frequency determines  $\lambda$ . The short period orbits are not used in this investigation, so for long period orbits:

$$\lambda = \sqrt{\frac{\sqrt{1 - 27\mu(1 - \mu)} - 1}{2}}. \quad (3.51)$$

For consistency,  $y_0$  is chosen to be the  $y$ -value of the Lagrange point  $y_L$  with  $\eta = 0$ . The initial guess for the period is also determined by the choice of frequency:

$$\tau = 2\pi s. \quad (3.52)$$

## Converged Equilateral Long Period Orbit Families

Since the CR3BP is symmetric about the  $xz$ -plane, all  $L_4$  orbit families can be mirrored across that plane to find the  $L_5$  families and vice versa. This is done by flipping the signs

of  $y$ ,  $\dot{x}$ , and  $\dot{z}$ . Therefore, Figure 3.18 shows portions of both equilateral long period orbit families in the Earth-Moon system and Figure 3.19 shows their stability indices.

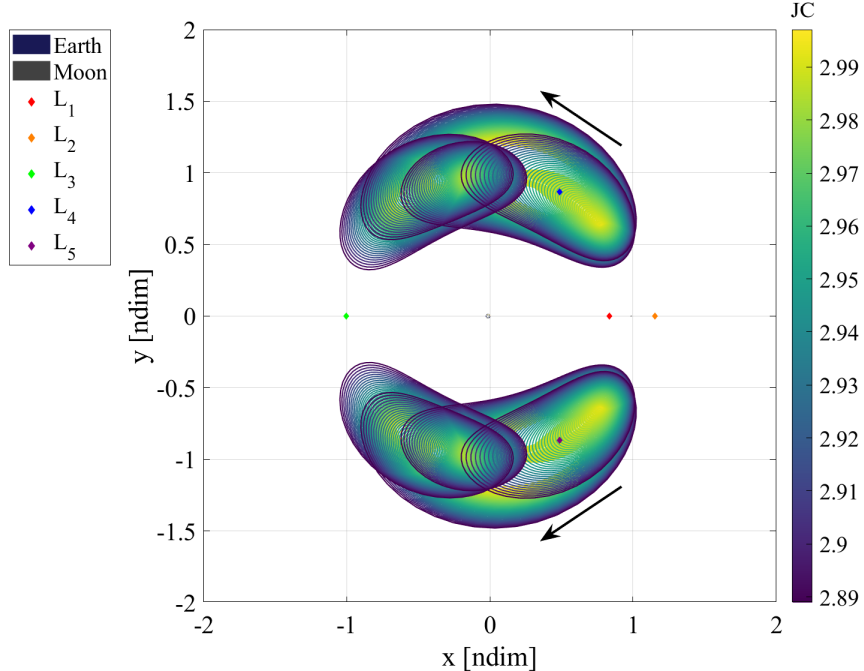


**Figure 3.18.** Earth-Moon  $L_4$  and  $L_5$  equilateral long period orbit families.

### 3.2.8 Equilateral Axial Orbits

#### A Spatial Equilateral Orbit Targeter

While axial orbits exist around  $L_4$  and  $L_5$ , unlike their colinear counterparts, these axial families bifurcate from the  $L_1$  halo family. Like the planar equilateral orbits, symmetry cannot be exploited to aid the targeting process, so periodicity must be targeted instead:

$$\bar{X} = \begin{bmatrix} x_0 & y_0 & \dot{x}_0 & \dot{y}_0 & \dot{z}_0 \tau \end{bmatrix}^T, \quad (3.53)$$

$$\bar{F}(\bar{X}) = \begin{bmatrix} x_f - x_0 & y_f - y_0 & \dot{x}_f - \dot{x}_0 & \dot{y}_f - \dot{y}_0 & \dot{z}_f - \dot{z}_0 & C - C_d \end{bmatrix}^T = \bar{0}, \quad (3.54)$$

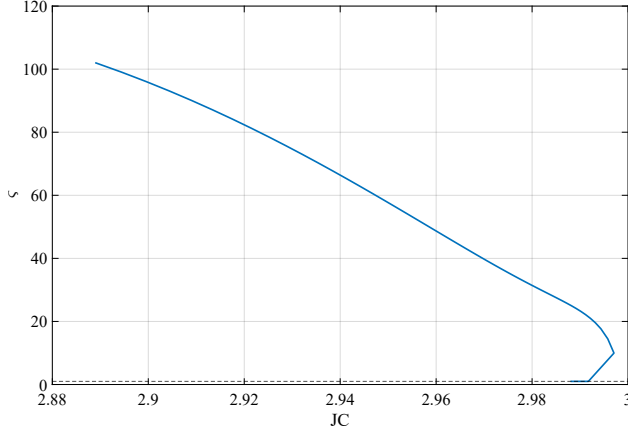


**Figure 3.19.** Earth-Moon equilateral long period orbit family stability index evolution.

$$DF(\bar{X}) =$$

$$\begin{bmatrix} \phi_{11} - 1 & \phi_{12} & \phi_{14} & \phi_{15} & \phi_{16} & \dot{x}_f \\ \phi_{21} & \phi_{22} - 1 & \phi_{24} & \phi_{25} & \phi_{26} & \dot{y}_f \\ \phi_{41} & \phi_{42} & \phi_{44} - 1 & \phi_{45} & \phi_{46} & \ddot{x}_f \\ \phi_{51} & \phi_{52} & \phi_{54} & \phi_{55} - 1 & \phi_{56} & \ddot{y}_f \\ \phi_{61} & \phi_{62} & \phi_{64} & \phi_{65} & \phi_{66} - 1 & \ddot{z}_f \\ 2x_0 - \frac{2(x_0 + \mu)(1 - \mu)}{d^3} - \frac{2\mu(x_0 - 1 + \mu)}{r^3} & 2y_0 - \frac{2y_0(1 - \mu)}{d^3} - \frac{2y_0\mu}{r^3} & -2\dot{x}_0 & -2\dot{y}_0 & -2\dot{z}_0 & 0 \end{bmatrix}. \quad (3.55)$$

### Converged Equilateral Axial Families

The pseudo-arc length method can be used to obtain the initial guess for the equilateral axial family. Stepping in one direction will produce the  $L_4$  family while stepping in the other produces the  $L_5$  family. These are both shown in Figure 3.20. Figure 3.21 shows the stability indices for these families. As hinted at by the end of these axial families,  $L_4$  and  $L_5$  vertical families also exist in the Earth-Moon system but are not used in this investigation.

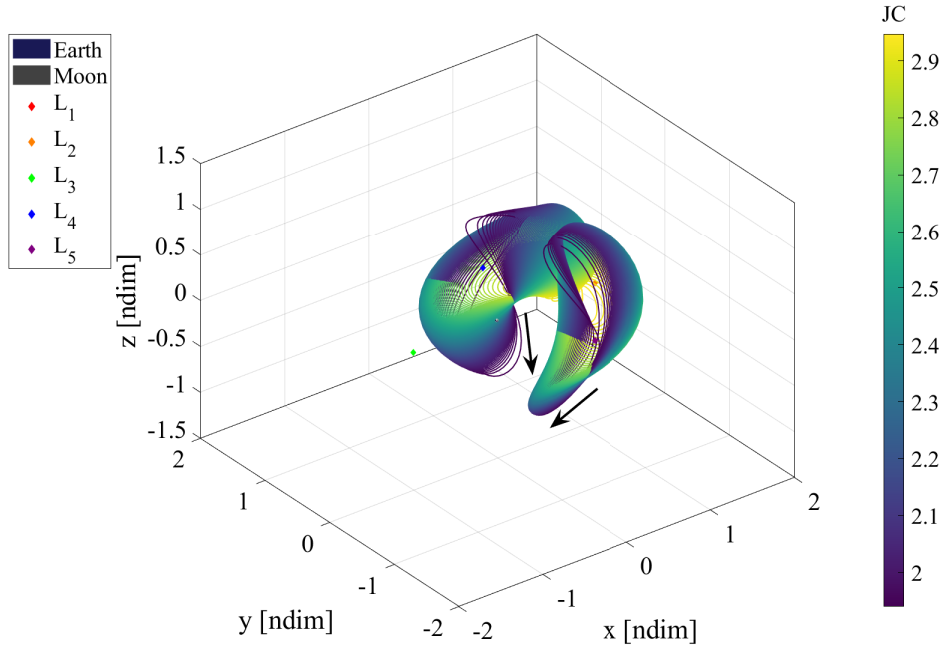


**Figure 3.20.** Earth-Moon  $L_4$  and  $L_5$  equilateral axial families.

### 3.2.9 Resonant Orbits

Many other types of CR3BP orbits are not associated with a Lagrange point. Some of these orbit families are known as resonant orbits because their periods are resonant or close to resonant with the Moon's' period. These orbits are still periodic in the rotating frame but are also periodic or close to periodic in an inertial frame. Individual orbits also tend to span more of the Earth-Moon system than the Lagrange point orbits. For more details on how to determine initial guesses and correct these orbits, Gupta[15] and Sadaka[16] provide extensive overviews and initial conditions. A couple of unstable resonant orbit families are used in this investigation and so they are shown here.

#### Converged 2:1a Resonant Orbit Family

The unstable section of the 2:1 resonant orbit family (denoted the 2:1a resonant orbit family by Sadaka) is shown in Figure 3.22[16]. These orbits travel around the Earth roughly twice for every time the Moon revolves around it, which becomes more evident when the

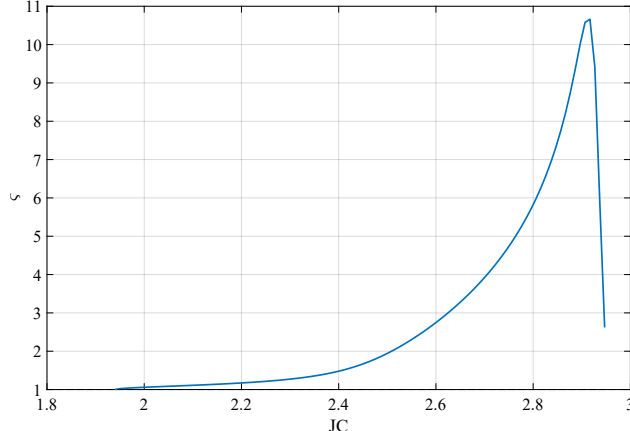


**Figure 3.21.** Earth-Moon equilateral axial family stability index evolution.

trajectories are viewed in an inertial frame. Figure 3.23 shows the stability index evolution for this family.

### Converged 3:4 Resonant Orbit Family

Another unstable family is the 3:4 resonant orbits, shown in Figure 3.24. These orbits go around the Earth three times for every time the Moon goes around. Their stability indices are given in Figure 3.25.

### 3.3 Invariant Manifolds

Dynamically unstable periodic orbits in the CR3BP have useful structures called invariant manifolds that represent the local flow near the orbit. With applications for transfer design, trajectories along these manifold surfaces can be used to ballistically arrive at or depart from the periodic orbit. Perko provides the following theorem for stable/unstable manifolds for periodic orbits[17]:

Let  $f \in C^1(E)$  where  $E$  is an open subset of  $R^n$  containing a periodic orbit,

$$\Gamma : \bar{x} = \gamma(t), \quad (3.56)$$

of  $\dot{\bar{x}} = f(\bar{x})$  of period  $T$ . Let  $\phi_t$  be the flow of  $\dot{\bar{x}} = f(\bar{x})$  and  $\gamma(t) = \phi_t(\bar{x}_0)$ . If  $k$  of the characteristic exponents of  $\gamma(t)$  have negative real part where  $0 \leq k \leq n - 1$

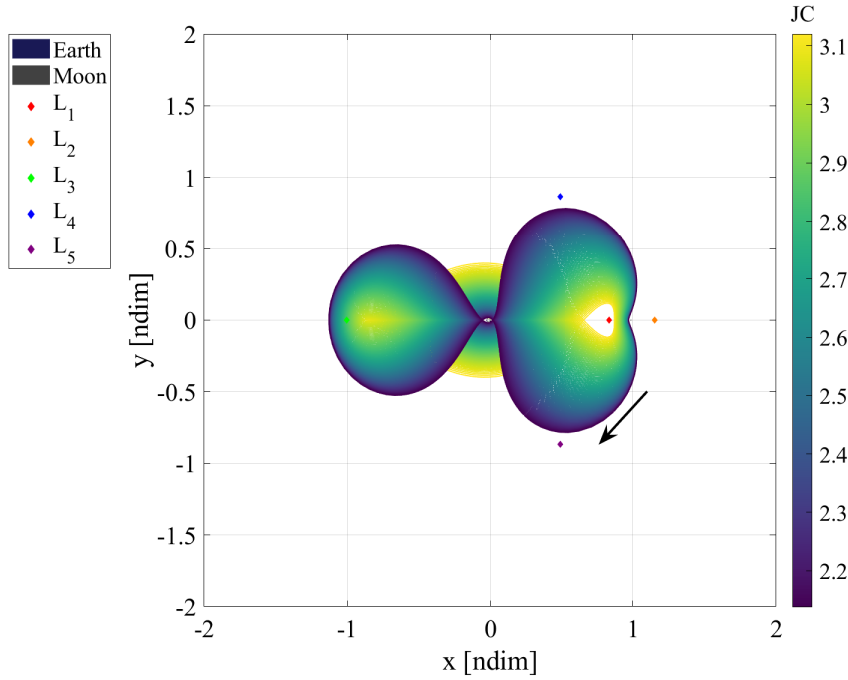


**Figure 3.22.** Earth-Moon 2:1a resonant orbit family.

and  $n - k - 1$  of them have positive real part then there is a  $\delta > 0$  such that the stable manifold of  $\Gamma$ ,

$$S(\Gamma) = \{\bar{x} \in N_\delta(\Gamma) | d(\phi_t(\bar{x}), \Gamma) \rightarrow 0 \text{ as } t \rightarrow \infty \text{ and } \phi_t(\bar{x}) \in N_\delta(\Gamma) \text{ for } t \geq 0\}, \quad (3.57)$$

is a  $(k + 1)$ -dimensional, differentiable manifold which is positively invariant under the flow  $\phi_t$  and the unstable manifold of  $\Gamma$ ,

$$U(\Gamma) = \{\bar{x} \in N_\delta(\Gamma) | d(\phi_t(\bar{x}), \Gamma) \rightarrow 0 \text{ as } t \rightarrow -\infty \text{ and } \phi_t(\bar{x}) \in N_\delta(\Gamma) \text{ for } t \leq 0\}, \quad (3.58)$$

is an  $(n - k)$ -dimensional, differentiable manifold which is negatively invariant under the flow  $\phi_t$ . Furthermore, the stable and unstable manifolds of  $\Gamma$  intersect transversally in  $\Gamma$ .

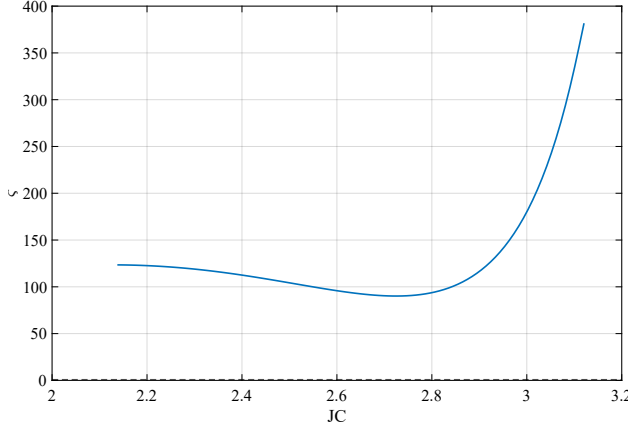


**Figure 3.23.** Earth-Moon 2:1a resonant orbit family stability index evolution.

In layman's terms, if a periodic orbit is unstable (has eigenvalues greater than and lesser than 1), then stable/unstable manifold surfaces exist that approach/leave the orbit asymptotically in forward time.

Since these manifold structures asymptotically depart the orbit structure, no deterministic maneuver is required to transfer onto them. However, a consequence of this is that it is not possible to identify the exact location along the orbit from where a manifold trajectory departs. Therefore, a numerical process is necessary to approximate the stable/unstable subspace of the orbit to determine an appropriate initial condition for an arc along the manifold surface.

Near the periodic orbit, the manifolds are tangent to their corresponding eigenspaces of the orbit. For a selected point on the periodic orbit:

$$\bar{\nu}(t_0 + t) = \Phi(t_0 + t, t_0)\bar{\nu}(t_0), \quad (3.59)$$

where  $\bar{\nu}(t_0)$  is the eigenvector at the initial condition corresponding to the stable or unstable eigenvalue of the monodromy matrix. Once the stable/unstable eigenvector at the selected point has been obtained:

$$\bar{\nu}_n = \frac{\bar{\nu}}{\sqrt{\nu_x^2 + \nu_y^2 + \nu_z^2}}, \quad (3.60)$$

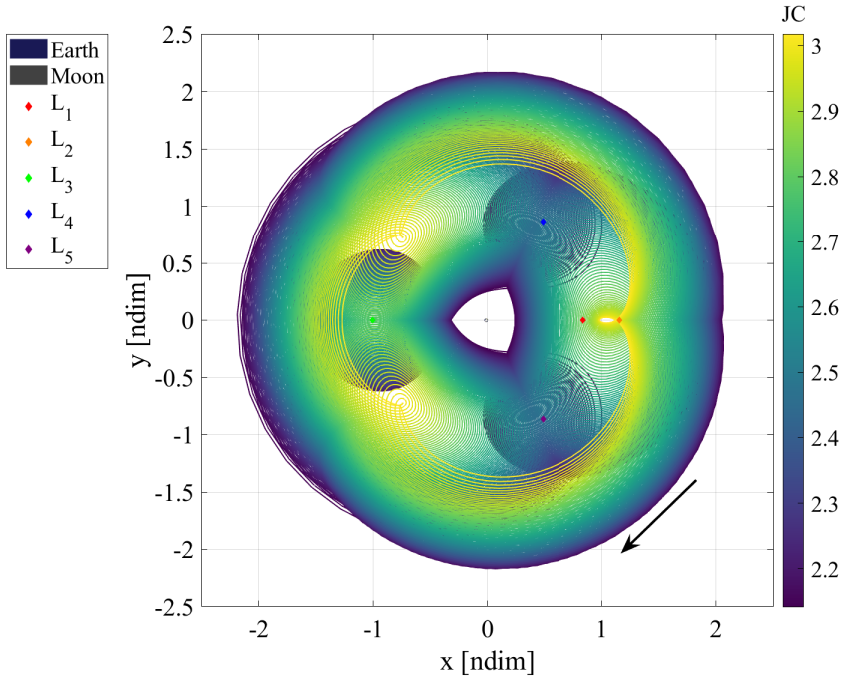


**Figure 3.24.** Earth-Moon 3:4 resonant orbit family.

where  $\nu_x$  is the  $x$ -component of the eigenvector and  $\bar{\nu}_n$  is the eigenvector normalized by the nondimensional distance from the selected point. Using the normalized stable eigenvector to approximate the initial condition for a stable manifold arc:

$$\bar{q}^S = \bar{q}_\Gamma \pm d\bar{\nu}_n^S, \quad (3.61)$$

where  $\bar{q}_\Gamma$  is the state vector at the selected point along the periodic orbit and  $d$  is a step-off distance, generally chosen based on the specific CR3BP system. The scaled eigenvector can be either added to or subtracted from the periodic state as the eigenspace is bi-directional, creating two half-manifolds for each stability. To compute an initial condition for an unstable manifold arc, use Equation (3.59)-Equation (3.61), replacing the stable components for unstable ones. Stable manifold arcs are then propagated backwards in time from the initial condition (arriving at the orbit in forward time) while unstable arcs are propagated forward in time from their initial condition.

As mentioned, the value for  $d$  depends on the CR3BP system in use. This parameter needs to be sufficiently small to well approximate the manifold structure. However, if  $d$  is

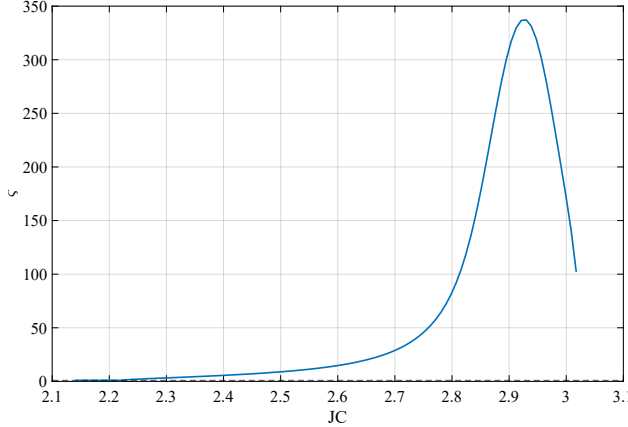


**Figure 3.25.** Earth-Moon 3:4 resonant orbit family stability index evolution.

too small, the trajectory will take longer than reasonable to arrive at/depart from the orbit since the dynamics are asymptotic[18]. Table 3.1 shows the values of  $d$  used for the systems in this investigation. As some examples of manifold structures, Figure 3.26 and Figure 3.27 show the stable and unstable manifolds for a planar Lyapunov orbit and a spatial halo orbit, respectively, in the Earth-Moon system. Each figure also shows a single manifold arc overlayed on the full structure for reference. A more thorough explanation of manifold theory can be found in Perko[17].

**Table 3.1.** Manifold Step-Off Distance Values of Relevant CR3BP Systems

CR3BP System	$d$ [km]
Earth-Moon	25
Sun-Earth	1000
Sun-Mars	1000

### 3.4 Poincaré Maps

Since plots of invariant manifolds in configuration space can be complex and do not display any velocity information about the trajectories, a different visualization technique is advantageous. Poincaré maps are an approach that concisely visualize trajectories by reducing the dimension of the problem through a hyperplane. These hyperplanes can be physical surfaces, like a plane or sphere in configuration space, or more abstract, like an apse

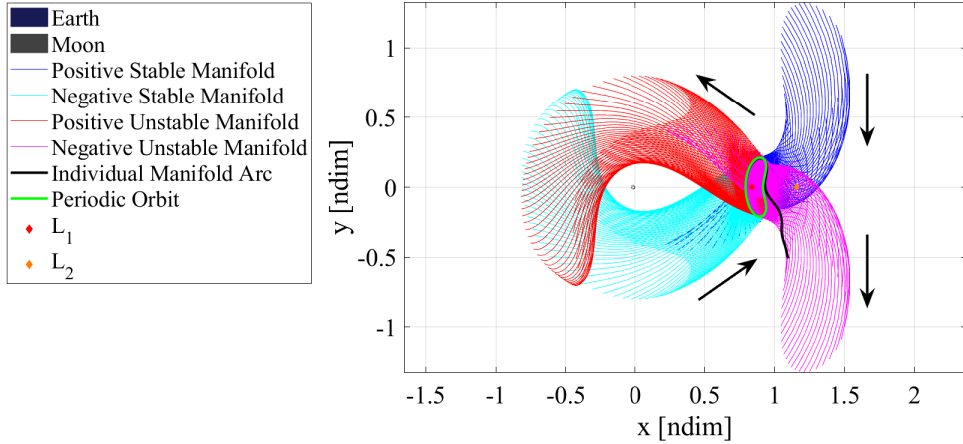


**Figure 3.26.** Earth-Moon  $L_1$  Lyapunov Manifolds ( $C = 3.05$ ).

or velocity map. As initial conditions are propagated, whenever a trajectory passes through the hyperplane, its crossing is marked on the Poincaré map. A simple example is shown in Figure 3.28.

Starting from an initial condition  $x_0$  on the hyperplane  $\Sigma$ , after propagating the trajectory returns to the hyperplane at  $P(x_0)$ . If the trajectory is precisely periodic, the trajectory will return to the same point,  $x^{PO}$ . The Poincaré map then is the 2-dimensional representation of the hyperplane, displaying only the trajectory crossings. Note that the axes of the map need not be position components but could also be velocity, energy, etc. Similar mappings are used in this investigation to more efficiently analyze and compare manifold trajectories of different orbits.

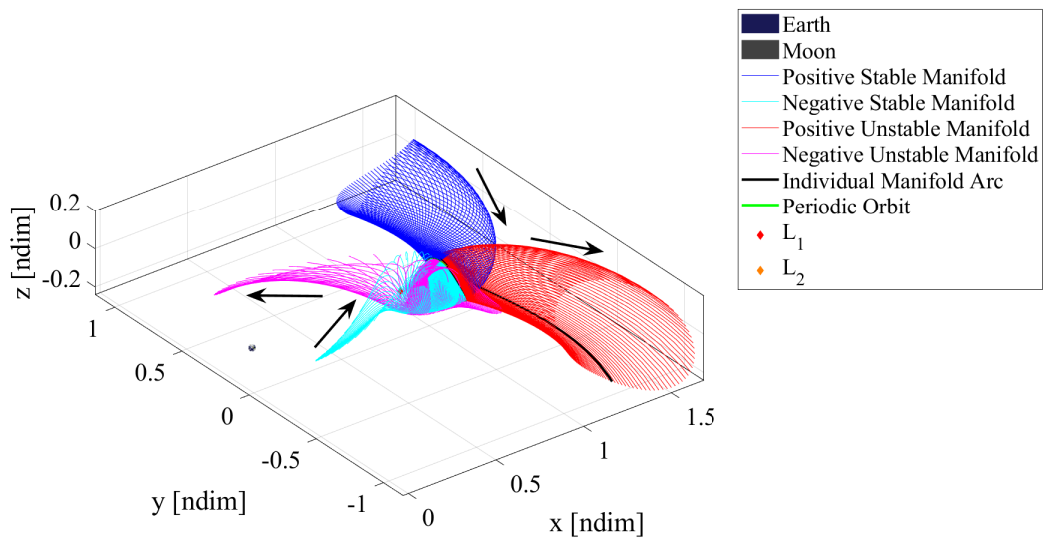


**Figure 3.27.** Earth-Moon  $L_2$  Halo Manifolds ( $C = 3.08$ ).

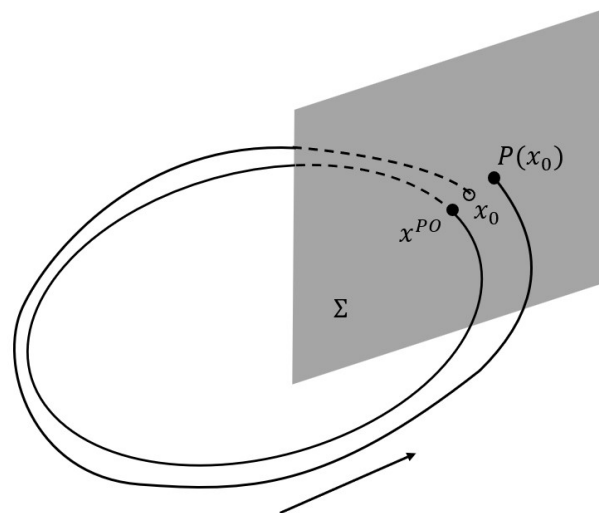


**Figure 3.28.** Poincaré map.

## 4. TRAJECTORY CONSTRUCTION

4.1 2BP Lambert Arcs

4.2 The Moon-to-Moon Analytical Transfer Method

4.3 Ballistic Transfers between Earth-Moon and Sun-Earth Systems

4.4 Flyby Targeting

## **5. END-TO-END MARS TRANSFERS**

**5.1 Transfers via Intermediate Sun-Earth Halos**

**5.2 Direct Transfers with Flybys**

## **6. CONCLUSION**

## REFERENCES

- [1] K. C. Howell, “Three-dimensional, periodic, ‘halo’ orbits,” *Celestial Mechanics*, vol. 32, no. 1, pp. 53–71, 1984. DOI: [10.1007/BF01358403](https://doi.org/10.1007/BF01358403).
- [2] B. Semenov, *Spice: An observation geometry system for space science missions*, 2023. [Online]. Available: <https://naif.jpl.nasa.gov/naif/>.
- [3] D. A. Vallado, *Fundamentals of Astrodynamics and Applications*, Fourth Edition. Hawthorne, CA, USA: Microcosm Press, 2013.
- [4] D. C. Garcia, “Transfer design methodology between neighborhoods of planetary moons in the circular restricted three-body problem,” Ph.D. Dissertation, Purdue University, West Lafayette, IN, USA, 2021.
- [5] E. M. Zimovan, “Characteristics and design strategies for near rectilinear halo orbits within the earth-moon system,” M.S. Thesis, Purdue University, West Lafayette, IN, USA, 2017.
- [6] K. K. Boudad, K. C. Howell, and D. C. Davis, “Departure and escape dynamics from the near rectilinear halo orbits in the earth-moon-sun system,” *The Journal of the Astronautical Sciences*, 2022. DOI: [10.1007/s40295-022-00328-w](https://doi.org/10.1007/s40295-022-00328-w).
- [7] K. K. Boudad, “Disposal dynamics from the vicinity of near rectilinear halo orbits in the earth-moon-sun system,” M.S. Thesis, Purdue University, West Lafayette, IN, USA, 2018.
- [8] D. J. Scheeres, “The restricted hill four-body problem with applications to the earth-moon-sun system,” *Celestial Mechanics and Dynamical Astronomy*, vol. 70, pp. 75–98, 1998. DOI: [10.1023/A:1026498608950](https://doi.org/10.1023/A:1026498608950).
- [9] M. A. Andreu, “Dynamics in the center manifold around l2 in the quasi-bicircular problem,” *Celestial Mechanics and Dynamical Astronomy*, vol. 84, pp. 105–133, 2002. DOI: [10.1023/A:1019979414586](https://doi.org/10.1023/A:1019979414586).
- [10] M. Kakoi, K. C. Howell, and D. Folta, “Access to mars from earth-moon libration point orbits: Manifold and direct options,” *Acta Astronautica*, vol. 102, pp. 269–286, 2014. DOI: [10.1016/j.actaastro.2014.06.010](https://doi.org/10.1016/j.actaastro.2014.06.010).

- [11] J. S. Parker and R. L. Anderson, *Low-Energy Lunar Trajectory Design*. Pasadena, CA, USA: NASA Jet Propulsion Laboratory, 2013.
- [12] R. Park, *Three-body periodic orbits*. [Online]. Available: [https://ssd.jpl.nasa.gov/tools/periodic\\_orbits.html](https://ssd.jpl.nasa.gov/tools/periodic_orbits.html).
- [13] E. M. Z. Spreen, “Trajectory design and targeting for applications to the exploration program in cislunar space,” Ph.D. Dissertation, Purdue University, West Lafayette, IN, USA, 2021.
- [14] R. J. Power, “Characterization of lunar access relative to cislunar orbits,” M.S. Thesis, Purdue University, West Lafayette, IN, USA, 2019.
- [15] M. Gupta, “Finding order in chaos: Resonant orbits and poincaré sections,” M.S. Thesis, Purdue University, West Lafayette, IN, USA, 2020.
- [16] N. I. Sadaka, “There and back again: Generating repeating transfers using resonant structures,” M.S. Thesis, Purdue University, West Lafayette, IN, USA, 2023.
- [17] L. Perko, *Differential Equations and Dynamical Systems*, Third Edition. New York City, NY, USA: Springer, 1991.
- [18] M. Kakoi, “Design of transfers from earth-moon  $L_1/L_2$  libration point orbits to a destination object,” Ph.D. Dissertation, Purdue University, West Lafayette, IN, USA, 2015.